Available online at www.sciencedirect.com

ScienceDirect

Geochimica et Cosmochimica Acta 258 (2019) 207–225

Geochimica et Cosmochimica Acta

www.elsevier.com/locate/gca

Extraterrestrial organic matter preserved in 3.33 Ga sediments from Barberton, South Africa

Didier Gourier [a,*], Laurent Binet [a], Thomas Calligaro [f,a], Serena Cappelli [a], Hervé Vezin [b], Jean Bréhéret [c], Keyron Hickman-Lewis [d,g], Pascale Gautret [e], Frédéric Foucher [d], Kathy Campbell [d], Frances Westall [d]

[a] Chimie ParisTech, PSL University, CNRS, Institut de Recherche de Chimie de Paris (IRCP), F-75005 Paris, France
[b] University Lille, CNRS, UMR 8516 – LASIR - Laboratoire de Spectrochimie Infrarouge et Raman, F-59000 Lille, France
[c] GéoHydrosystèmes Continentaux (GéHCO), EA 6293, Université de Tours, Parc de Grandmont, F-37200 Tours, France
[d] Centre de Biophysique Moléculaire (CBM), CNRS, F-45071 Orléans, France
[e] Université d'Orléans BRGM, CNRS, Institut des Sciences de la Terre d'Orléans (ISTO), 45060 Orléans, France
[f] Centre de Recherche et de Restauration des Musées de France (C2RMF), Palais du Louvre, F-75001 Paris, France
[g] Dipartimento di Scienze Biologiche, Geologiche e Ambientali, Università di Bologna, Via Zamboni 67, I-40126 Bologna, Italy

Received 20 September 2018; accepted in revised form 6 May 2019; Available online 15 May 2019

Abstract

Electron paramagnetic resonance (EPR) analysis of carbonaceous, volcanic, tidal sediments from the 3.33 Ga-old Josefsdal Chert (Kromberg Formation, Barberton Greenstone Belt), documents the presence of two types of insoluble organic matter (IOM): (1) IOM similar to that previously found in Archean cherts from numerous other sedimentary rocks in the world and of purported biogenic origin; (2) anomalous IOM localized in a 2 mm-thick sedimentary horizon. Detailed analysis by continuous-wave-EPR and pulse-EPR reveals that IOM in this layer is similar to the insoluble component of the hydrogenated organic matter in carbonaceous chondrites, suggesting that this narrow sedimentary horizon has preserved organic matter of extraterrestrial origin. This conclusion is supported by the presence in this thin layer of another anomalous EPR signal at $g = 3$ attributed to Ni-Cr-Al ferrite spinel nanoparticles, which are known to form during atmospheric entry of cosmic objects. From this EPR analysis, it was deduced that the anomalous sedimentary layer originates from deposition, in a nearshore environment, of a cloud of tiny dust particles originating from a flux of micrometeorites falling through the oxygen-poor Archean atmosphere.

Keywords: Extraterrestrial organic matter; Spinels; Electron paramagnetic resonance; Early Archean; Josefsdal chert formation

1. INTRODUCTION

It is widely believed that most of the water and organic matter on the Hadean Eon (4.54–4 Ga) was of extraterrestrial material (Morbidelli et al., 2012; Marty et al., 2013 and references therein). While recent models suggest that the majority of extraterrestrial flux occurred before 4.4 Ga (Boehnke and Harrison, 2016; Genda et al., 2017), there is nonetheless evidence for continued input of extraterrestrial material throughout the Early Archaean (~4–3.2 Ga). For example, Schoenberg et al. (2002) document evidence for meteoritic input through tungsten isotope

* Corresponding author.
E-mail address: didier.gourier@chimieparistech.psl.eu (D. Gourier).

https://doi.org/10.1016/j.gca.2019.05.009
0016-7037/

analysis of 3.7 Ga metamorphosed sediments from Isua, Greenland, while a number of layers of impact spherules have been observed in Early-Mid Archean (~3.5–3.2 Ga) sediments from the Barberton Greenstone Belt (South Africa) and the Pilbara Craton (Western Australia) (Glikson et al., 2004; Gomes et al., 2005; Krull-Davatzes et al., 2010; Bottke et al., 2012; Lowe et al., 2014). This flux still continues today, albeit to a lesser extent (e.g., Love and Brownlee, 1991; Yada et al., 2004).

Extraterrestrial material may have provided substantial sources of complex organic molecules for the emergence of life (e.g. Cooper et al., 2001; Strasdeit, 2005; Pasek and Lauretta, 2008). Organic matter in carbonaceous chondrites can reach up to 4% (Sephton, 2002) and up to 85% in ultracarbonaceous micrometeorites (Duprat et al., 2010; Dartois et al., 2018). About 75% of organic matter in carbonaceous chondrites is refractory, consisting mostly of small aromatic moieties linked by short and branched aliphatic chains (Derenne and Robert, 2010). This insoluble component will hereafter be referred to as insoluble organic matter (IOM). Although representing only a small fraction, soluble components exhibit a vast range of composition, with more than 14,000 different molecules containing C, H, O, N and S having been identified to date (Schmitt-Kopplin et al., 2010; Remusat, 2014). Meteoritic debris and micrometeorites falling into the ocean of the early Earth would have been rapidly broken up and partially dissolved in the globally acidic and warm ocean (Pinti, 2005; Tartèse et al., 2017), thus liberating both the soluble and the refractory fractions (Westall et al., 2018). The soluble molecules would be rapidly dissolved into seawater whereas the refractory materials (the IOM) would remain in the detrital fraction of the volcanic sediments coating the floor of the ocean and the numerous platform-covering (submerged continents) shallow seas. Of particular interest is the fate of this latter fraction, its potential involvement in prebiotic reactions leading to the emergence of life, and its distinction from organic biosignatures of ancient traces of life. In this study, we describe evidence of the oldest traces of extraterrestrial organic matter yet identified through a detailed, sedimentological, geochemical, and Electron Paramagnetic Resonance (EPR) study of Early Archaean (3.33 Ga) sediments in the Barberton Greenstone Belt (BGB). These results will certainly have implications for the search for organic biosignatures of primitive life on Earth and on Mars

2. THE JOSEFSDAL CHERT AND ITS SEDIMENTOLOGICAL CONTEXT

The 3.33 Ga Josefsdal Chert (the stratigraphic equivalent of unit K3c in the Kromberg Formation), located in the southern part of the Barberton Greenstone Belt (Fig. 1A) (Lowe et al., 2012) is an extensive deposit of mostly basaltic volcanic sediments deposited on top of hydrothermally silicified basalts extruded onto a shallow water platform (Westall et al., 2006, 2011, 2015). The 7 m to up to 20 m thick deposit (variations in thickness depending upon underlying, fault-bounded topography) is divided into four stratigraphical units denoted 1–4 comprising four recurring lithological facies denoted A, B, C and D (Westall et al., 2015) (Fig. 1B). The sedimentological structures and textures indicate deposition in an initially regressive environment from upper offshore to upper shore face (supratidal), followed by a transgressive sequence back to shoreface/foreshore. The sediments are highly silicified (85.5–99.9%), the silicification occurring more or less contemporaneously with deposition. The clastic sediments comprise volcanic protoliths including lithic fragments of basalt, volcanic glass, accretionary lapilli, minerals such as feldspar laths, pyroxene remnants, rare spherulites, as well as carbon of both demonstrably biogenic and detrital origins. The lithic fragments are generally highly altered to muscovite and anatase and replaced by silica, although some remnant structures such as tear-drop shapes, remain. Chemical deposits in the form of silica gels are both intercalated with the detrital sediments as a cement and form layers precipitated on top of bedding planes.

Biogenic features have been documented in various degrees of abundance throughout the sedimentary succession (Westall et al., 2006, 2011, 2015). They comprise the carbonaceous and silicified remains of delicate phototrophic biofilms and mats formed atop sediment layers, as well as densely clotted mats of thickly colonized volcanic particles. Biogenicity interpretations were made on the basis of morphology, carbonaceous composition, carbon isotopic signature consistent with microbial fractionation, molecular composition (as determined by ToF-SIMS), all within a specific context defined on the mineralogic to local geological environment. Further details regarding methodology and discussion of biogenicity criteria are detailed in the above published papers.

We here concentrate on Facies D of Unit 3 in the Josefsdal Chert (Fig. 1), and use a black chert from Facies C only for comparison. Unit 3, from which the studied samples are sourced, is bounded below and above by conspicuous layers of intraformational breccia. Facies D comprises finely laminated green/grey and black sediments (ranging from mm's to cm's in thickness) consisting of repetitive bundles of volcanic ash and fine accretionary lapilli deposited as parallel, graded beds, the tops of which are delineated by very fine carbonaceous laminae. The carbonaceous component represents deposition in relatively quiet periods between ashfall episodes (Supplementary Fig. A1). Intermittent remobilization of the sediments by current and wave action resulted in cross bedding and oscillatory bedding, the lamina bundles being bounded between two of such deposits. These sedimentary structures, as well as mud cracks (not shown), are suggestive of an upper shore face (subtidal-tidal) environment in which the sediments were occasionally subjected to subaerial exposure. The fact that it is possible to trace individual layers, even the thinnest laminae (mm-thickness), over distances of several kilometers (Westall et al., 2015) suggests that deposition was of regional scale from ash fall with only occasional current reworking, i.e. during quiescent hydrodynamic regimes. In addition to the underlying and overlying breccia layers, Facies D exhibits evidence of more significant disturbance in the form of slumping and a certain amount of blurring of the sedimentary structures indicating liquefaction. These structures

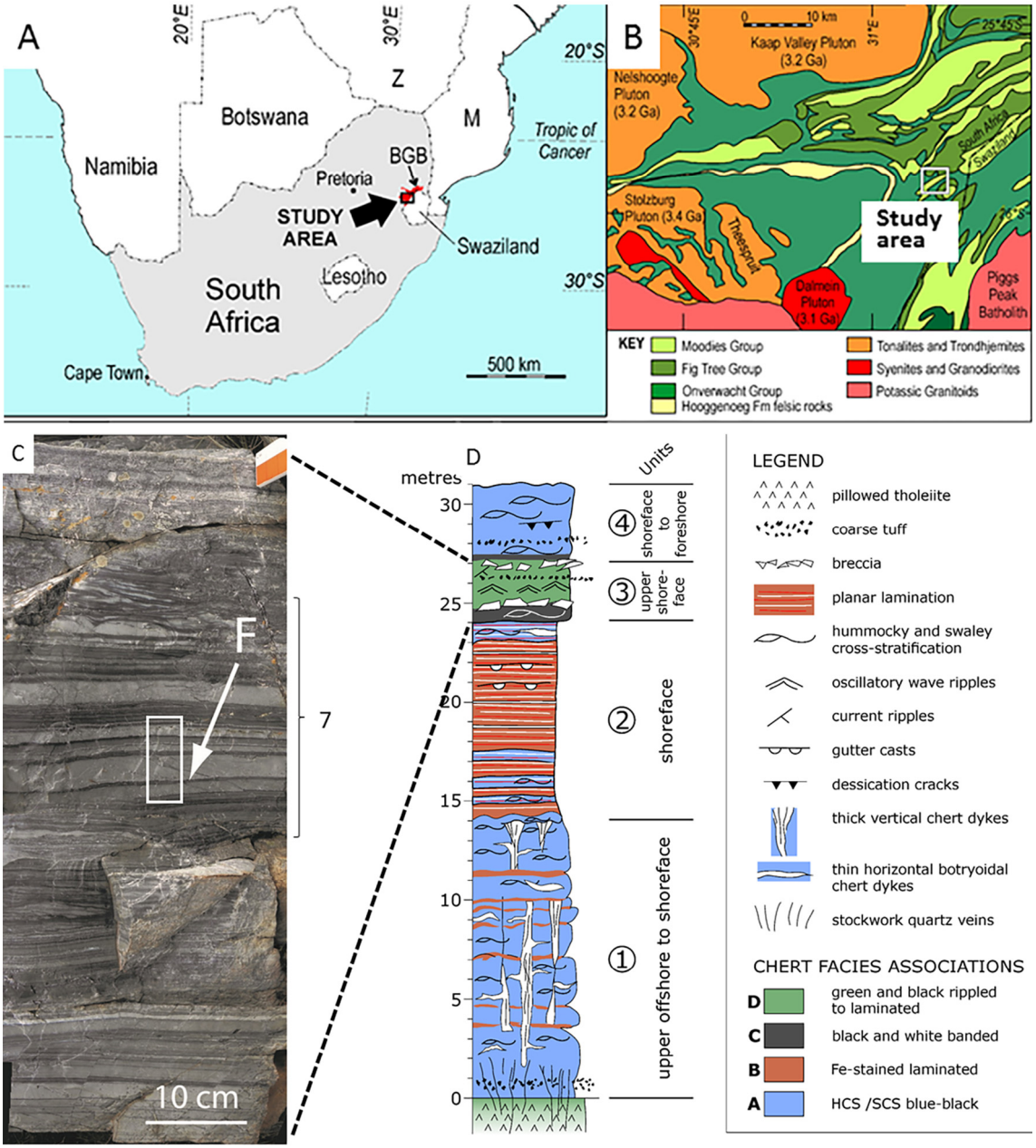

Fig. 1. Location and stratigraphy of the 3.33 Ga Josefsdal Chert in the Barberton Greenstone Belt (BGB), South Africa. (A) Geographical and geological location of the BGB and (B) location of the studied area within the southern part of the BGB (after Westall et al. (2015)). (C) Composite field photographs of Facies D, occurring in Unit 3 (Fig. 1D), in which the carbonaceous layer F of interest to this study is marked by a white arrow. The sample analysed and shown in Fig. 4 is located by a rectangular box in this image. Facies D comprises a series of finely laminated, graded tuff layers, bounded by wave/current reworked intervals. Carbonaceous layer F occurs in the 7th bundle of tuff layers (group marked as 7). (D) Generalized stratigraphic column with sedimentary units noted 1–4 with their environmental assignations. The facies associations A–D are noted by different colors.

were caused by shocks, possibly seismic and/or explosive hydrothermal events.

Of the eight bundles of laminae comprising the Facies D strata of Unit 3, the horizon labelled F in Fig. 1D, occurring towards the base of the 7th bundle, is the main focus of our attention in this study (Supplementary Fig. A2). Horizon F is a 2 mm thick composite carbonaceous layer that formed at the top of a graded tuffaceous bed. It comprises three separate, carbon-rich laminae (labelled F′, F″, and F‴ in Fig. 2). As shown in this paper, lamina F′ is the one in which the EPR peak indicating extraterrestrial organic matter is strongest. This 200–300 μm thick lamina is a mixture of carbonaceous matter, highly altered and silicified spherical clasts (accretionary lapilli and both barred and structureless spherulites), and includes a small component (<0.2%) of minute pyrite

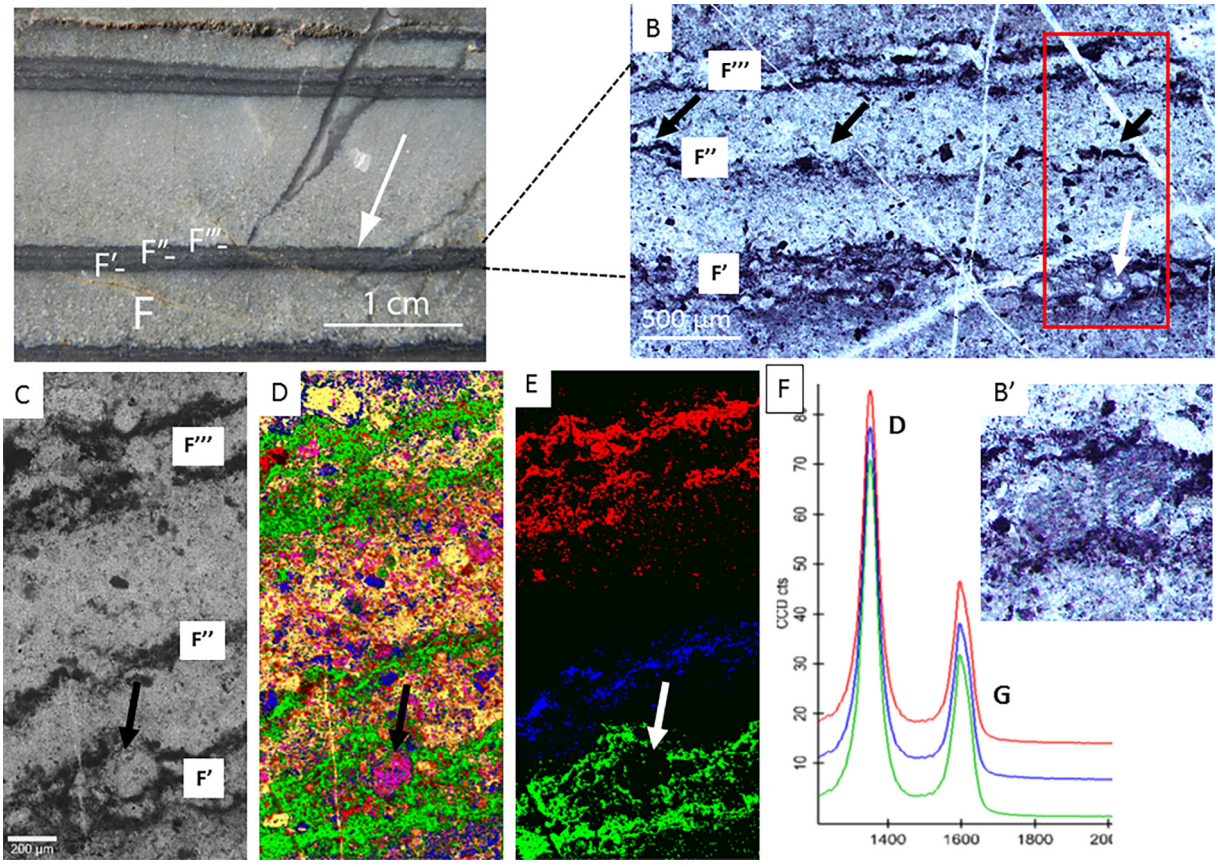

Fig. 2. Sedimentological detail of horizon F. (A) Outcrop detail showing that horizon F occurs between two layers of graded tuffaceous sediments. It consists of three laminae, labelled F′, F″, F‴. (B) Optical microscope view of a thin section (60 µm) of horizon F showing that laminae F′ and F‴ comprise spherulite-rich layers with intermixed carbonaceous matter, as well as fine, undulating carbonaceous laminae below and above. Lamina F″, on the other hand, is thinner and laterally discontinuous. The red box denotes the area analyzed by Raman spectroscopy (D, E). The white arrow marks the location of a prominent, altered spherule visible in (B–E). (B′) The inset shows spherules in lamina F′ having a barred texture, similar to extraterrestrial spherules described by Simonson and Glass (2004). (C) Optical detail of area mapped by Raman. (D) Combined composition of the mapped area. Carbon is in green, quartz in yellow/orange, muscovite in pink, anatase in blue. (E) The three carbonaceous laminae are highlighted in different colors (F′ in green, F″ in blue and F‴ in red). (F) Raman spectra of the respective three laminae F′, F″ and F‴ show that all spectral parameters are identical: D and G peaks are located at 1354 cm^{-1} and 1598 cm^{-1}; their full width at half maximum values are equal to 50 cm^{-1} and 57 cm^{-1} respectively, and the D/G intensity ratio is equal to 2.2. (For interpretation of the references to colour in this figure legend, the reader is referred to the web version of this article.)

crystallites. It is separated from the second carbonaceous lamina (F″) by about 400 µm of tuffaceous sediments. Lamina F″ is very fine (~50 µm), undulating and laterally discontinuous (Fig. 2B). A 600 µm tuffaceous layer separates lamina F″ from the third carbonaceous lamina F‴ which, like F′, is a mixture of altered spherulites and carbonaceous matter (Fig. 2B).

3. SAMPLES AND METHODS

3.1. Samples

Samples were obtained during numerous field campaigns. Dedicated field work to elucidate the geological context was undertaken in 2012 and 2014. Two samples, collected in upper shoreface facies C and D of unit 3 (Fig. 1) were selected for study by EPR. The first sample, labelled α (size 5.7 cm × 2 cm) was collected from the tuffaceous layer of Facies D marked by an arrow in Fig. 1C. This sample, shown in Figs. 4 and 6, contains four of the eight black horizons of the 7th bundle, labelled E, F, G and H, horizon F being the carbonaceous horizon of interest in this study. It was cut for EPR analysis into 40 slices (1–1.5 mm width; numbered from 0 to 39) parallel to the sedimentation plane. The second sample (~3 cm × 2 cm), labelled β, was collected from the homogenous and relatively carbon-rich Facies C, which underlies Facies D (Fig. 1D). It was used as a reference for the EPR signature of carbonaceous matter in the Josefsdal Chert in general. It was polished and cut into 27 strips (section 2 × 2 mm^2, 3–8 mm length) for EPR analysis (see Fig. 6).

3.2. Methods

Thin sections of the same samples were made for optical microscopy and Raman analyses. Optical microscopy was

conducted on 30–60 μm polished thin sections using an Olympus BX51 microscope at the CNRS-CBM (Orléans). Raman analyses were undertaken at CNRS-CBM (Orléans) on the polished thin sections using a WITec Alpha500 RA Raman spectrometer equipped with green laser (frequency-doubled Nd:YAG laser at 532 nm) and a Nikon E Plan 50x objective of numerical aperture 0.75. The analysis was conducted with the method described by Foucher et al. (2017), with a laser power chosen to have an energy density lower than 1 mJ/μm^3 to prevent sample heating. Raman mapping was carried out on a sample containing horizon F collected close to the sample α location, but not sample α itself. The reason for this separate analysis was to avoid perturbations of the organic matter of the black horizon F by the Raman laser beam, which would invariably modify the EPR spectrum of IOM. The Raman analysis documents the pervasive alteration of the volcanic protoliths to muscovite and anatase/rutile followed by significant silicification (>85–96% SiO_2) (Westall et al., 2018). Carbonaceous matter was concentrated in the horizon F laminae (Fig. 2C–E). Raman spectra of minerals in horizon are given in Supplementary Fig. B1. In detail, Raman spectroscopy also shows that the carbonaceous component is finely disseminated between the volcanic clasts in lamina F′ and F‴. The very thin lamina F″ comprised primarily carbonaceous matter (IOM) in a quartz matrix. Lamina F″ is absent in sample α. Parameters of the Raman spectra show that there are no differences in peak position, shape, width and I_D/I_G ratio of D and G Raman bands of the IOM in the three horizons (Fig. 2F).

Elemental micromapping of sample α was carried out using Particle Induced X-ray Emission (PIXE) ion microprobe analysis (Ryan, 1995) at the *Accelerator Grand Louvre for Elemental Analysis* (AGLAE) of the *Centre de Recherche et de Restauration des Musées de France* (C2RMF) located in the Palais du Louvre, Paris (Calligaro et al., 2011). A rectangular area of 5 × 0.5 mm^2 from horizon F was scanned at a resolution of 20 μm using a 3-MeV proton beam of ~30 μm diameter extracted in the air through a 100-nm thick Si_3N_4 membrane, yielding maps of 250 × 25 points. Three 50-mm^2 SDD detectors (Ketek AXAS-A) were placed 20 mm from the sample at 50° relative to the beam axis and screened with 100-μm Al absorber foils to collect trace element X-rays (Z > 20). An additional detector without absorber fitted with a magnetic deflector in a helium gas flow at 2 litre/min was used to record bulk element X-rays, mainly Si, S and Fe required for the trace element calibration. Each PIXE spectrum was collected with a proton dose of 32 nC. The mean beam intensity was 16 nA and the total mapping time was 3.5 h. Count rates in major elements and trace element detectors were 20 and 1.5 kcounts/sec, respectively. Hence pile-up was negligible. The acquired spectra were processed to obtain quantitative composition using the TRAUPIX program (Pichon et al., 2014) built upon the GUPIX software package (Campbell et al., 2010). Processing parameters were adjusted using the Diorite DR-N reference geostandard (Govindaraju, 1982). It is important to note that this PIXE analysis was performed on the remaining part of sample α after the collection of the 40 slices for EPR analyses. This precaution was necessary to avoid any change to the IOM by the ion beam, which would invariably perturb the EPR signatures.

Continuous wave EPR spectra (cw-EPR) were recorded at the X-band (≈9.4 GHz) and at room temperature using a Bruker ELEXSYS E500 spectrometer equipped with a 4122SHQE/011 resonator. The 67 fragments of cherts were separately introduced into EPR quartz tubes for cw-EPR analysis. Pulsed-EPR experiments were carried out at 5 K with a Bruker ELEXSYS E500 X-band spectrometer equipped with a Bruker cryostat "cryofree" system. Hyperfine Sublevel Correlation pulse sequence (HYSCORE) was used to reveal interactions of the electron spins of carbonaceous matter with ^{13}C ($I = 1/2$; 1.1 % abundance), ^{1}H ($I = 1/2$; 100% abundance), and ^{31}P ($I = 1/2$; 100% abundance) nuclei. Using this technique, a spin echo is generated by the pulse sequence $\pi/2$-τ-$\pi/2$-t_1-π-t_2-$\pi/2$-τ-*echo*. The angles $\pi/2$ and π represent the flip angles of the electron magnetization. Its intensity is measured by varying the times t_1 and t_2 at constant time τ in a stepwise manner. The lengths of the $\pi/2$ and π pulses were fixed at 16 ns and 32 ns, respectively. 256 × 256 data points were collected for both t_1 and t_2 at increments of 20 ns. τ value was set at 136 ns for all samples. The unmodulated part of the echo was removed by using second-order polynomial background subtraction. The magnitude spectrum was obtained after 2D Fourier transformation of the spectra by using a Hamming apodization function. Pulse-EPR analysis was performed on slice 25 of sample α and fragment 9 of the carbon-rich sample β (see Fig. 6). For sample α, due to weak echo signal even at 5 K, the spectrum consists in 100 accumulations with 100 shots per points. Original EPR and PIXE data are given in Electronic annexes.

4. RESULTS

4.1. General EPR features of Josefsdal chert

The EPR spectra of the 40 slices of the laminated chert (sample α) vary significantly according to their stratigraphic (vertical) position. Fig. 3 shows two examples of EPR spectra corresponding to slice 33 (located above black horizon E) and slice 25 which contains lamina F′ of horizon F. The locations of these slices in the sample are shown in Fig. 4. Slice 33 (Fig. 3A and B) is lithologically representative of the bulk sample, except for the relative intensity of the EPR signals, which varies from slice to slice. The most prominent feature in Fig. 3A is a broad symmetrical line at $g \approx 2$ which broadens and distorts at low temperature (not shown). This peculiar temperature dependence indicates that this signal corresponds to the resonance signal of superparamagnetic (SPM) nanoparticles, possibly ferrites. Such particles become ferrimagnetic at low temperature, which is responsible for the broadening, shifting and distortion of the line (Griscom, 1980, 1984). At low magnetic field, an EPR line at $g = 4.3$ is typical of Fe^{3+} impurities in low symmetry sites of inorganic hosts. Zooming in the high field portion of the SPM line reveals four additional EPR signals (Fig. 3B). The weak narrow line at $g = 2.003$, noted as IOM on the diagram, is due to carbonaceous

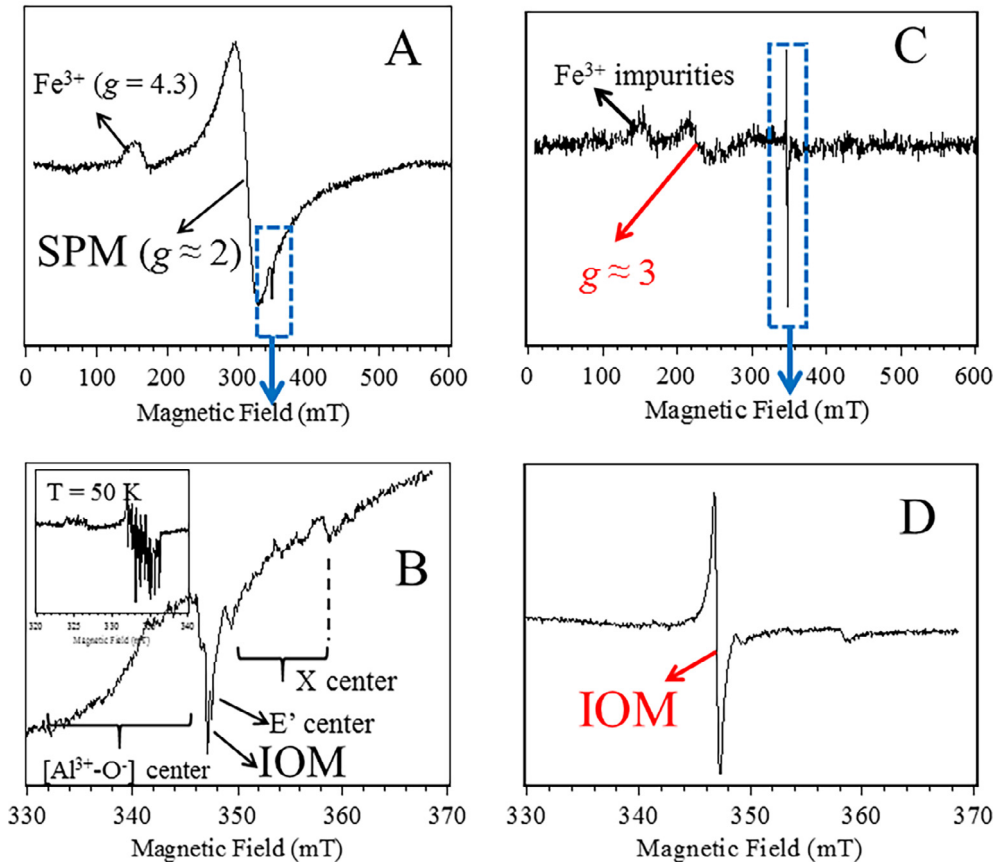

Fig. 3. cw-EPR spectra of two representative fragments of sample α: slice 33 (A and B) and slice 25 (C and D). (A) Full range EPR spectrum of slice 33 showing Fe^{3+} impurities and a strong signal of superparamagnetic resonance (SPM) at $g \approx 2$ due to the presence of magnetic nanoparticles. The rectangular box represents the part of the EPR spectrum detailed in (B), which shows the weak line of carbonaceous matter (IOM), the E′ center and the Al^{3+}-O^{-} center. The spectrum of the latter recorded at 50 K is shown in the inset, where the hyperfine interaction with the ^{27}Al nucleus is clearly seen. (C) Total EPR spectrum of slice 25, corresponding to lamina F′ of horizon F. The rectangular box represents the part of the EPR spectrum detailed in (D), which shows the IOM line. The two EPR signals that present extraterrestrial characteristics (the IOM line and the SPM signal at $g = 3$) are represented in red. Experimental conditions: microwave power 10 mW, modulation depth 0.1 mT, microwave frequencies 9.7443 GHz (spectra A and B), 9.7418 GHz (spectra C and D); inset of panel B: microwave power 2 mW, modulation depth 0.1 mT, microwave frequency 9.3924 GHz. (For interpretation of the references to colour in this figure legend, the reader is referred to the web version of this article.)

matter (Skrzypczak-Bonduelle et al., 2008). A narrow peak in the high field flank of this IOM line is due to oxygen vacancy centers (E′ centers) in the SiO_2 matrix (see Weil, 1984; Weeks et al., 2008 and references therein). This attribution to E′ centers was demonstrated by the fact that the E′ line can be detected selectively by recording the EPR spectrum 90° out-of-phase with the modulation field (not shown), which is not the case for other EPR signals (Skrzypczak-Bonduelle et al., 2008). A broad and unresolved signal is also visible in the low field side of the IOM line, which is best resolved by recording the EPR spectrum at 50 K (insert in Fig. 3B). This signal exhibits a characteristic structure due to hyperfine interaction with ^{27}Al nuclei (nuclear spin $I = 5/2$) and three components, $g_z = 2.0060$ $g_x = 2.0085$ and $g_y = 2.003$, of the g-factor. This was also observed in carbonaceous cherts of the Warrawoona Group, Pilbara Craton, Australia (Skrzypczak-Bonduelle et al., 2008). This paramagnetic center is an (O^{-}-Al^{3+}) center, resulting from hole trapping by an oxygen ion (i.e a O^{-} center) adjacent to an Al^{3+} impurity in Si site of a silicate matrix (Weil, 1984, Botis and Pan, 2009). Note that the aluminum is most probably related to the presence of muscovite, the lower greenschist-metamorphic variant of smectite, a common, aqueous alteration product of volcanic detrital precursors that was subsequently silicified (Westall et al., 2015). In the high magnetic field part of the spectrum, a doublet of EPR lines is due to an as yet unidentified center (referred to as the X center) in the mineral matrix, and will not be discussed further in this paper as it is ubiquitous in the sample.

The EPR spectrum of slice 25 (Fig. 3C), corresponding mostly to lamina F′ of horizon F, exhibits unusual features compared to other slices of sample α. First, the SPM signal of superparamagnetic nanoparticles ($g = 2$) is lacking and the IOM line of carbonaceous matter is more intense. Second, in addition to the signal at $g = 4.3$ of Fe^{3+} impurities, present throughout in the sample, there is another signal at $g = 3$, which is of particular interest because it was clearly

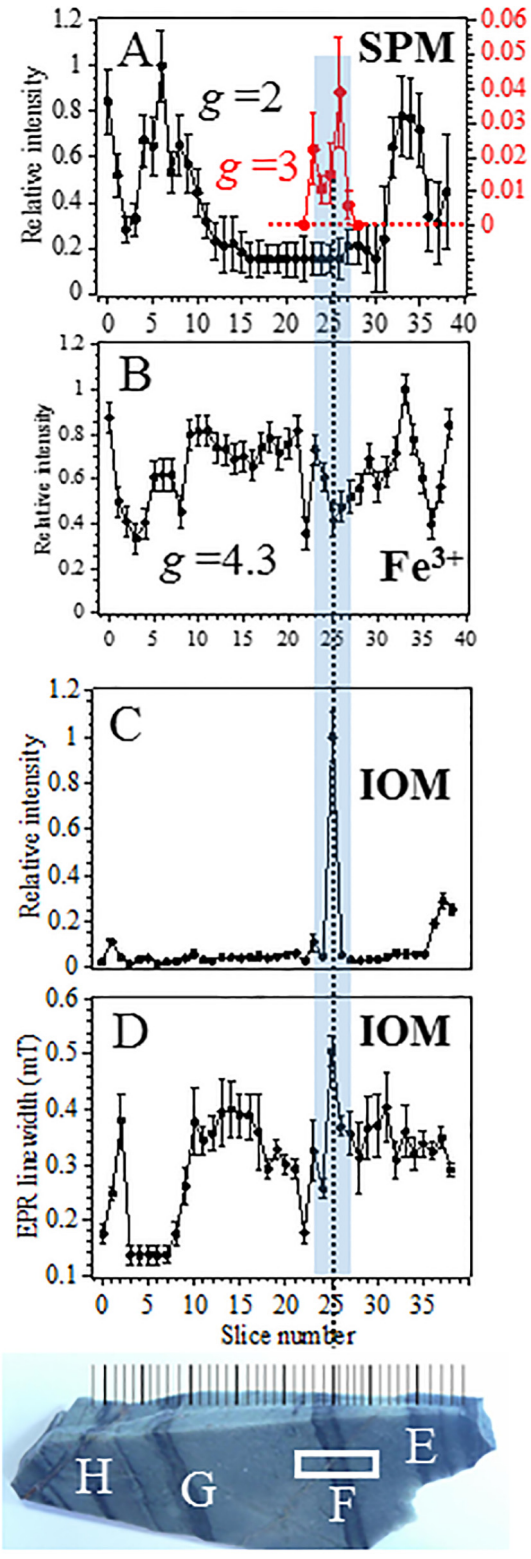

observed only in horizon F of sample α (slices 23–26). The central part of the spectrum (blue box in Fig. 3C) clearly shows the IOM line as well as the undetermined X center (Fig. 3D).

The heterogeneity of sample α is reflected in the strong variability of the EPR spectra throughout the 40 slices. Fig. 4 presents the weight normalized EPR intensity profile of four EPR signals: the SPM signals at $g = 2$ and $g = 3$ (Fig. 4A), the signal of Fe^{3+} impurities at $g = 4.3$ (Fig. 4B) and the IOM line (Fig. 4C). The peak-to-peak linewidth of the IOM line is shown in Fig. 4D. The slice number is given in abscissa. EPR intensities of each type of EPR signal are given in arbitrary units, which do not reflect their abundance. For example, Fe^{3+} impurities in mineral hosts (signal $g = 4.3$) are present everywhere in the sample, but their average concentration is low (probably no more than 100 ppm) because the total Fe content in the bulk of sample α (except F horizon) is less than 1000 ppm. On the contrary, SPM particles are inhomogeneously distributed. The SPM signal at $g = 2$ is present only in slices 0–12 and slices 30–36, corresponding to the black horizons G-H and E, respectively (Fig. 4A). Interestingly, the signal at $g = 3$ (in red in Fig. 4A) is observed only in slices 23–26, corresponding to the black horizon F, which also contains an anomalous IOM line. This will provide a focus for discussion in the following sections.

4.2. EPR lineshape analysis of carbonaceous matter

EPR associated with carbonaceous matter (IOM) have long been studied, for example in ancient carbonaceous material such as coal (Uebersfeld and Erb, 1956; Retcofsky et al., 1968; Mrozowski, 1988a,b), carbonaceous cherts (Skrzypczak-Bonduelle et al., 2008; Bourbin et al., 2013), and carbonaceous chondrites (Duchesne et al., 1964; Vinogradov et al., 1964; Schultz and Elofson, 1965;

Fig. 4. Variation of cw-EPR spectra in the 40 slices of sample α shown at the bottom of the diagram (the location of this sample in the context of the outcrop is shown by a rectangle in Fig. 1C). The slices, labelled 0–39 along the abscissa of (D), were collected parallel to the stratification. In terms of stratigraphy, slice 0 (to the left) corresponds to the stratigraphic top of the sample and slice 39 to the bottom (to the right). The image of sample α is shown with the position of the 40 slices studied by EPR (vertical bars) and four black horizons (labelled E to H). The white box represents the area scanned in the PIXE analysis (see Section 4.4.1). Data for the black horizon F (slices 23–26) are highlighted with a blue rectangle covering panels A–D. Slice 25 comprises a large part of lamina F′ of horizon F and is highlighted by a discontinuous vertical line. (A) EPR intensity profile of the superparamagnetic resonance signal (SPM) of possibly ferrite nanoparticles ($g = 2$), and of the signal at $g = 3$ attributed to Ni-Cr-Al ferrite nanoparticles; (B) EPR intensity profile of Fe^{3+} impurities ($g = 4.3$), (C) EPR intensity profile of the IOM line; (D) Variation of the peak-to-peak linewidth of the IOM line. All intensities are given in arbitrary units. (For interpretation of the references to colour in this figure legend, the reader is referred to the web version of this article.)

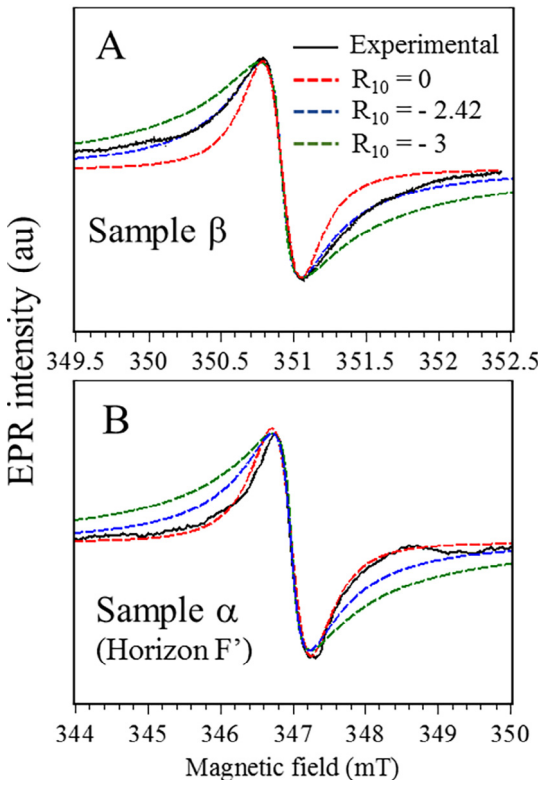

Fig. 5. EPR line of carbonaceous matter (IOM) in slice 17 of sample β (A) and slice 25 (mostly lamina F′) of sample α (B). The experimental spectrum (black line) is compared with calculated spectra (dashed lines) corresponding to Lorentzian ($R_{10} = 0$, red) and stretched Lorentzian profiles with $R_{10} = -2.42$ (blue) and $R_{10} = -3$ (green). (For interpretation of the references to colour in this figure legend, the reader is referred to the web version of this article.)

Binet et al., 2002, 2004; Gourier et al., 2008; Delpoux et al., 2011). These carbonaceous materials invariably give a single EPR line due to aromatic radical moieties with an unpaired electron spin delocalized in π-type molecular orbitals (Uebersfeld et al., 1954; Retcofsky et al., 1968; Mrozowski, 1988b; Dickneider et al., 1997). The IOM line can be characterized by its intensity (proportional to the number of radicals), its *g*-factor (measured from the magnetic field at resonance) and its lineshape.

Compared to the homogenous, carbon-rich black chert (sample β, Figs. 5A and 6) that is used as a reference and which exhibits a sharp IOM line, the laminated chert (sample α) has only a weak IOM line, even in the black horizons G, H and E. The IOM line is relatively strong only in slice 25, which mainly corresponds to lamina F′ of black horizon F (Figs. 4C and 5B). The peak-to-peak linewidth ΔB_{pp} of the IOM line also varies across the sample, as shown in Fig. 4D. Three different linewidth domains can be distinguished. The IOM lines of the majority of sample α are characterized by ΔB_{pp} in the range of 0.25–0.4 mT, which agrees with values of 0.2–0.3 mT previously measured in ~3.4 Ga-old cherts from the BGB (Skrzypczak-Bonduelle et al., 2008). The IOM line in slices 3–7 exhibits a very narrow linewidth $\Delta B_{pp} = 0.13$ mT, previously observed in a 3.48 Ga-old chert from the Dresser Formation (Warrawoona Group, Australia) (Skrzypczak-Bonduelle et al., 2008). In contrast, the IOM line of slice 25, dominated by lamina F′, has a linewidth $\Delta B_{pp} = 0.5 \pm 0.02$ mT, which exceeds the largest linewidth previously measured in Archean cherts but corresponds to the values $\Delta B_{pp} = 0.38$–0.54 measured for the IOM line in carbonaceous chondrites (Binet et al., 2002, 2004). The broadening of the IOM line can be ascribed to two different origins. For Phanerozoic, Proterozoic and meteoritic IOM, the linewidth is determined by the hydrogen/carbon ratio, while for Archean carbonaceous matter, the linewidth is mainly determined by the metamorphic grade (Binet et al., 2002; Skrzypczak-Bonduelle et al., 2008).

Additional information on the origin of this IOM can be obtained from analysis of the IOM lineshape. We have previously observed that the shape of IOM lines in carbonaceous cherts varies from Gaussian-Lorentzian (Voigt shape) to Lorentzian for ages ranging from Phanerozoic to Proterozoic, then to stretched Lorentzian for ages dating back to Archean. Skrzypczak-Bonduelle et al. (2008) proposed a numerical analysis of the IOM line by deriving a lineshape parameter (noted R_{10}) defined to quantify the deviation of the signal from a Lorentzian shape (see Skrzypczak-Bonduelle et al., 2008; Bourbin et al., 2013 for more detail). Briefly, the lineshape parameter is characterized by values $R_{10} = 0$ for a pure Lorentzian line, $R_{10} > 0$ for an increasing Gaussian character, and $-3 < R_{10} < 0$ for a stretched Lorentzian line. Fig. 5 shows the analysis of two IOM lines, corresponding to slice 25 of the laminated chert α (lamina F′ of black horizon F), and to a representative fragment of the carbon-rich chert β. Both experimental spectra are compared with a Lorentzian line ($R_{10} = 0$) and two stretched Lorentzian lines ($R_{10} = -2.42$ and -3). The IOM line of chert α (slice 25) is close to Lorentzian (Fig. 5B), while the Lorentzian is clearly stretched in chert β, with $R_{10} = -2.42$ (Fig. 5A).

From lineshape parameters R_{10} and linewidths ΔB_{pp} collected from previous EPR analyses of Precambrian cherts (Skrzypczak-Bonduelle et al., 2008; Bourbin et al., 2013) and carbonaceous chondrites (Binet et al., 2002, 2004), we constructed an EPR diagram of primitive carbonaceous matter, plotting the lineshape parameter R_{10} versus the linewidth parameter ΔB_{pp} (Fig. 6). Open circles labelled by letters *a* to *l* represent samples collected from different geological settings and chondrites, detailed in the caption of Fig. 6. Archean, Proterozoic and meteoritic IOMs are distributed in three different domains in this diagram, highlighted by colored rectangles. Archean IOM (blue area) is characterized by a stretched Lorentzian shape ($-2 \leq R_{10} \leq -3$), while Proterozoic IOM (orange area) is characterized by a shape close to the Lorentzian ($-1 \leq R_{10} \leq +1$). Meteoritic IOM (green area) and Proterozoic IOM have similar lineshapes but different linewidths, that of meteorites being higher. It is important to note that the EPR of most Phanerozoic IOM (younger than 450 Ma) fall out of the field of this phase diagram, as demonstrated by the 45 Ma Clarno sample (Fig. 6, data point i), because the EPR signal of organic matter in such

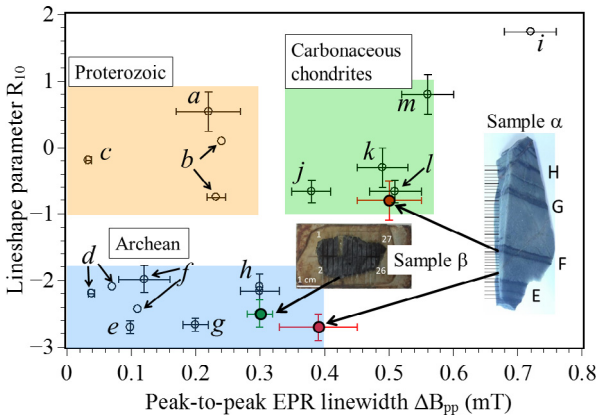

Fig. 6. EPR lineshape factor R_{10} versus peak-to-peak linewidth ΔB_{pp} of IOM lines for carbonaceous chondrites and Precambrian cherts (open circles, data from Skrzypczak-Bonduelle et al., 2008; Bourbin et al., 2013; Binet et al., 2002, 2004), and for IOM line in sample β (green circle) and sample α (red circles, slices 25 and 33) of Josefsdal Chert. The diagram is constructed from data obtained for the following samples: (*a*) Dahongyu Formation, Hebei, China (1.43–1.77 Ga); (*b*) Gunflint Formation, Shreiber Beach locality, Ontario, Canada (1.88 Ga); (*c*) Duck Creek, Wyloo Group, Ashburton Trough, Australia (1.85–2.2 Ga); (*d*) Jeerinah Formation, Fortescue Group, Hamersley basin, Australia (2.75 Ga); (*e*) Middle Marker, Komati Formation, Barberton Greenstone Belt, South Africa (3.47 Ga); (f) Dresser Formation, Warrawoona Group, Pilbara craton, Australia (3.48 Ga); (*g*) Kromberg Formation, Upper Onverwacht Group, Barberton Greenstone Belt, South Africa (3.42–3.45 Ga); (*h*) Middle Marker, Komati Formation, Barberton Greenstone Belts, South Africa (3.47 Ga); (*i*) Clarno Formation, John Day Basin Tectonic Unit, Oregon, USA (0.045 Ga); (*j*) Orgueil meteorite; (*k*) Paris meteorite; (*l*) Murchison meteorite; (*m*) Tagish Lake meteorite. The two images represent sample α (with black horizons E, F, G H), and sample β polished and cut in 27 slices (slice 9 is missing). The error bars for sample β represent the dispersion of the values measured for the 27 slices. (For interpretation of the references to colour in this figure legend, the reader is referred to the web version of this article.)

samples often exhibits a resolved hyperfine interaction with hydrogen nuclei, giving a multi-line EPR pattern (Skrzypczak-Bonduelle et al., 2008).

Data from the Josefsdal cherts in Fig. 6 suggest that some of the IOM of samples β (facies C) and α (facies D) has different origins. First, the values measured for the 27 slices of the carbon-rich sample β are almost identical and localized in the Archean part of the diagram (green circle in Fig. 6), the error bars representing the dispersion of experimental values. This result indicates that the structure and evolution of this IOM is similar to that of other Archean IOM in carbonaceous cherts from South Africa and Australia. On the contrary, data from the carbon-poor sample α are more widely scattered. Red circles in Fig. 6 represent experimental values for slices 25 and 33 of sample α. Although the IOM in slice 33 is at the outer edge of the domain covered by other Archean samples, its lineshape evidently corresponds to the stretched Lorentzian typical of Archean IOM. Surprisingly, the data for slice 25, consisting mainly of IOM from lamina F′, is located clearly outside the domain of Archean IOM and inside the field of carbonaceous chondrites.

This feature is a first indication of a possible extraterrestrial origin for the IOM in horizon F.

4.3. Pulse-EPR analysis of carbonaceous matter

The proposed extraterrestrial origin of the IOM in lamina F′ is supported by pulse-EPR analysis. Using Hyperfine Sublevel Correlation (HYSCORE) spectroscopy (Schweiger and Jeschke, 2001) we identified nuclei with non-zero nuclear spin (mainly ^{1}H, ^{13}C, ^{31}P) interacting with the electron spins of IOM radicals. Previous studies showed that meteoritic IOM and biogenic IOM in cherts exhibit different HYSCORE spectra resulting from different molecular structures and hydrogen contents, which in turn reflect their origin and diagenetic/metamorphic evolution (Gourier et al., 2008, 2010, 2013). Fig. 7 shows HYSCORE spectra of slice 25 of sample α (Fig. 7E) and a fragment of sample β (Fig. 7F) of the Josefsdal Chert, compared with IOM of the Orgueil meteorite (Fig. 7D), two carbonaceous cherts with indisputably biogenic IOM: Clarno Formation, Oregon, USA (Eocene, 0.045 Ga, Fig. 7A), Gunflint Formation, Ontario, Canada (Paleoproterozoic, 1.88 Ga, Fig. 7B), and one chert from the Dresser Formation of the Warrawoona Group, Pilbara, Australia (Archean, 3.48 Ga, Fig. 7C) (Gourier et al., 2008, 2013), with IOM of likely biogenic origin. HYSCORE spectra of Clarno and Gunflint cherts, which contain well-preserved fossils, show similar characteristics, namely (i) a non-linear hydrogen ridge centred at the nuclear frequency 14.5 MHz of ^{1}H, (ii) a very weak signal at the nuclear frequency 3.7 MHz of ^{13}C and (iii) a double-frequency signal at 12 MHz, which is twice the nuclear frequency 6 MHz of ^{31}P. Phosphorus is one of the bio-essential elements, and phosphate are also associated to fossil bacteria via biomineralization (Li et al., 2013; Cosmidis et al., 2015). So it is not surprising to detect ^{31}P resonance associated to carbonaceous fossils. HYSCORE spectra of meteoritic IOM from Orgueil differ from those of biogenic IOM by the presence of a linear ^{1}H ridge, a broad and intense ^{13}C ridge, and the lack of a double-frequency ^{31}P signal. The same features were observed for the Tagish Lake meteorite (Gourier et al., 2008, 2013). The differences observed for ^{1}H and ^{13}C signals are most probably related to the molecular structure of the IOM. Meteoritic IOM comprises small polyaromatic units linked by short and highly branched aliphatic moieties (Derenne and Robert, 2010), while biogenic IOM contains polyaromatic units with fewer branched aliphatic side chains (Gourier et al., 2013). The HYSCORE spectrum of the Archean chert of the Dresser Formation is clearly different from that of more recent cherts (Clarno and Gunflint Formations) due to the absence of the ^{1}H signal. This is because the hydrogen/carbon ratio decreases during the maturation of the IOM, approaching zero in mature Archean IOM. Thus, only the double-frequency signal of ^{31}P nuclei is present, suggesting that the IOM is derived from bacterial sources. The same spectroscopic characteristics observed for the 3.48 Ga Dresser Formation chert (Fig. 7C) are also clearly present in facies C (sample β) of the Josefsdal Chert (Fig. 7F), which shows

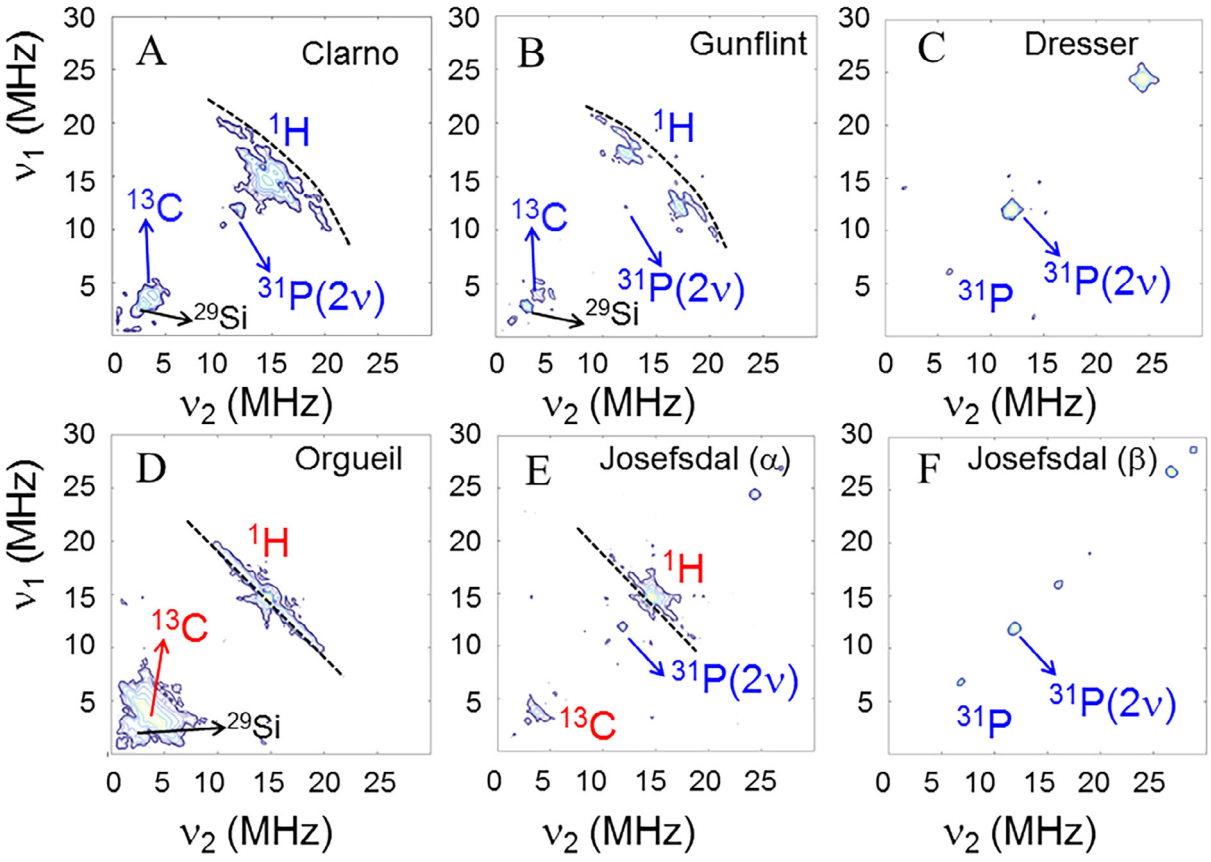

Fig. 7. HYSCORE spectra at 5 K of (A) a chert from the Clarno Formation, John Day Basin Tectonic Unit, Oregon, USA (0.045 Ga); (B) a chert from the Gunflint Formation, Schreiber Beach locality, Ontario, Canada (1.88 Ga); (C) a chert from the Dresser Formation, Warrawoona Group, Pilbara craton, Australia (3.48 Ga); (D) IOM of the Orgueil meteorite; (E) and (F) samples α and β, respectively, of the Josefsdal Chert, Barberton Greenstone Belt, South Africa. The dotted lines in A, B, D, E highlight the shape of the proton ridge in biogenic and meteoritic IOM. All 2D HYSCORE spectra were recorded at a τ value of 136 ns, with 256 × 256 points in both t_1 and t_2 dimensions.

only the ^{31}P signal. This result strongly suggests that the IOMs of these two Archean black cherts have a biological origin and underwent a similar metamorphic history. This biological origin of the IOM is well documented for the Josefsdal chert (Westall et al., 2015). On the contrary, the anomalous IOM present in slice 25 (horizon F′) of sample α exhibits a peculiar HYSCORE spectrum (Fig. 7E), with a combination of characteristics of biological and meteoritic IOMs. In particular, it shows the linear ^{1}H ridge and the extended and relatively intense signal of ^{13}C characteristic of chondritic IOM, while the double-frequency ^{31}P signal at 12 MHz is characteristic of fossilised IOM (Gourier et al., 2013).

In summary, two independent spectroscopic characteristics derived from cw-EPR and pulse-EPR measurements support the hypothesis that IOM of horizon F in sample α is a mixture of extraterrestrial hydrogenated organic matter and of biogenic dehydrogenated organic matter, the latter being present in small amounts throughout the sample.

4.4. Origin of the EPR signal at $g = 3$

In addition to the IOM EPR line presenting characteristics of extraterrestrial organic matter, horizon F (slices 23–26 of sample α) also features an EPR line at $g = 3$ (Fig. 3C). This signal does not appear in other slices of sample α, and was detected neither in the 27 fragments of sample β, nor in any carbonaceous cherts of various ages previously studied by EPR (Skrzypczak-Bonduelle et al., 2008). Examination of Fig. 4A (red symbols) shows that the intensity profile of the g = 3 signal through horizon F exhibits two maxima clearly corresponding to lamina F′ and F‴. The large deviation of the g-factor from the free electron value 2.0023 implies that the $g = 3$ signal cannot be due to organic radicals and must therefore be due to a mineral phase containing transition metals (Wertz and Bolton, 1986). Furthermore, to the best of our knowledge, g-values between 4.3 (Fe^{3+} impurities in low symmetry) and ≈2.3 (Ni^{2+} and Cu^{2+}) are rare in mineral compounds. Consequently, the presence of both extraterrestrial organic matter and an anomalous EPR signal at $g = 3$ in the same thin sedimentary horizon F prompted us to explore a possible extraterrestrial origin for this $g = 3$ signal. In favor of this hypothesis, spinel particles in the fusion crust of Allende meteorite give a signal with a large g-value ~2.5 (Griscom et al., 1999). Moreover Smart (1954) demonstrated that Ni-Fe-Al spinels can exhibit g-values covering the range 1.5–5.8 depending on their metal composition. In order to constrain the mineral compounds producing the signal at

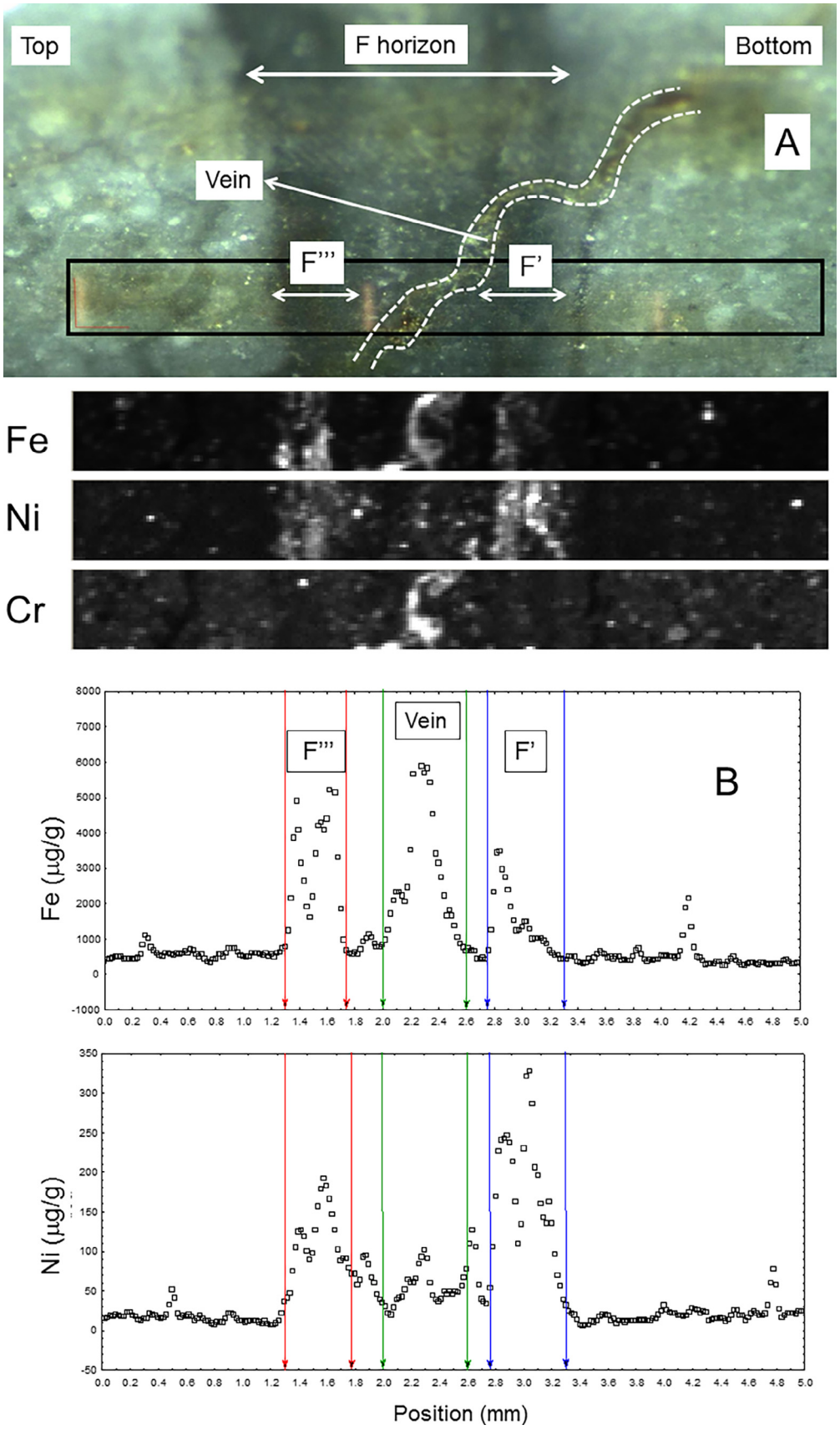
Top
F horizon
Bottom
A
Vein
F'''
F'
Fe
Ni
Cr
Vein
F'''
F'
B
Fe (µg/g)
Ni (µg/g)
Position (mm)

$g = 3$, the chemical composition of horizon F and the surrounding sedimentary horizons were analyzed by PIXE spectroscopy.

4.4.1. PIXE analysis of horizon F

The elemental composition of horizon F in sample α was mapped by the micro-PIXE method. The scanned area is represented by a white rectangular box in the optical image of sample α in Fig. 4, which corresponds approximately to slices 20–30 of the EPR analyses. The image in Fig. 8A is a magnified view of the same surface area of sample α as outlined in Fig. 4. A narrow chert vein (penecontemporaneous and possibly hydrothermal in origin) crossing lamina F′ and F‴ is visible in the rectangular box. Representative PIXE spectra of the vein, of laminae F′, F‴ and of a tuffaceous sediment are shown in Figs. C1–C4 of the Supplementary Information. Elemental maps for Fe, Ni and Cr qualitatively show that the vein is enriched in Fe and Cr, while laminae F′ and F‴ are enriched in Fe and Ni (Fig. 8A). In order to better determine the composition of these three domains, the 25 PIXE spectra recorded for each of the 250 horizontal positions (i.e. parallel to the stratification) were grouped together prior fitting in order to improve count statistics and S/N ratio without sacrificing horizontal resolution. The obtained sensitivity was 200 μg/g for S, 12 μg/g for Cr, 4 μg/g for Fe and 7 μg/g for Ni. The resulting 250-point elemental linescan across horizon F and the surrounding tuffaceous sediment was further examined by selecting three separated domains marked by vertical arrows in Fig. 8B. Data from these three domains are represented in the compositional plots in Fig. 9: lamina F‴ (red squares), vein (green diamonds), lamina F′ (blue triangles), and the surrounding tuffaceous layers referred to as the bulk (black dots). The Ni/Cr plot (Fig. 9A) allows a clear distinction to be made between the vein enriched in Cr and the F′ and F‴ laminae, which contain almost the same Cr content as the bulk. In contrast, the two laminae are characterized by higher Ni concentrations. While a previous Raman investigations reported the presence of small amounts of microcrystalline (<5μm) pyrite in the Josefsdal Cherts (Westall et al., 2015), the Fe/S plot of sample α shows that data for laminae F′ and F‴ and the vein clearly lie outside the domain occupied by iron sulphides (Fig. 9B). Furthermore, the Fe/Ni plot shows a marked distinction between the hydrothermal vein and the F′ and F‴ laminae (Fig. 9C). Since pyrite may be excluded as the principal iron bearing mineral in lamina F′ and F‴, it is more likely that Fe and Ni are mainly present in spinels as such compounds may exhibit large g-values (Smart, 1954).

4.4.2. The "cosmic" nanospinel model

Magnetic spinels are known to be formed in extraterrestrial objects during their entry in the Earth's atmosphere, and are sometimes referred to as cosmic spinels (Robin et al., 1992). Such spinels from large impacts have been identified in spherules at the Cretaceous-Tertiary (K-T) boundary (Montanari et al., 1983), as well as in Archean spherules beds from the BGB (Byerly and Lowe, 1994). They originate from liquid droplets formed at high temperatures that quenched into glassy spherules (Gayraud et al., 1996). Among other characteristics, cosmic spinels differ from terrestrial spinels by their higher Fe^{3+} and Ni, Cr contents (Smit and Kyte, 1984; Robin et al., 1992, 1993; Barnes and Roeder, 2001). However, apart from an EPR analysis of titanomagnetite nanoparticles in K-T spherules from the floor of the Chicxulub crater (Griscom et al., 1999), it seems that there have been no other EPR investigations of spinels related to extraterrestrial objects.

The general composition of spinel-type ferrites is $(M^{2+})^{A}(Fe_2^{3+})^{B}O_4$, where M represents a divalent metal. In normal spinels, divalent cations occupy the tetrahedral A-sites and trivalent cations the octahedral B-sites of the structure. In inverse spinels, half of the B-sites are occupied by the M^{2+} ions and the A-sites by Fe^{3+} ions, i.e. $(Fe^{3+})^{A}(M^{2+}Fe^{3+})^{B}O_4$. Spinel-type ferrites are generally ferrimagnetic compounds with the A-sites and B-sites constituting two antiferromagnetically coupled sublattices. The non-compensation of the magnetic moments of the A and B sublattices gives a net magnetic moment $\vec{M}$ per unit cell related to the total spin $\vec{S}$ of a unit cell by $\vec{M} = -g\beta\,\vec{S}$, where g is the g-factor and β the electron Bohr magneton. The magnetic moment and the total spin, hence the g-factor of spinel-type ferrites, are very sensitive to cationic distributions between the A and B sites. Consequently the g-factor can be used to determine the cation site occupancy in the structure (Gorter, 1954; Smart, 1954). In a standard electron magnetic resonance experiment, only the absolute value of the g-factor can be measured. The latter is given by Smart (1954):

$$|g| = \left| \frac{\left(\sum_i x_i g_i S_i\right)_A - \left(\sum_i x_i g_i S_i\right)_B}{\left(\sum_i x_i S_i\right)_A - \left(\sum_i x_i S_i\right)_B} \right| \quad (1)$$

where x_i, g_i, and S_i are the fractional occupancies, the g-factor and the spin quantum number of ion i in either A or B site, respectively.

Since Fe^{3+} in spinels may be partially substituted by Al^{3+} or Cr^{3+}, we considered a Ni-Cr-Al ferrite of composition $(Fe^{3+})^{A}(Fe_{1-x}^{2+}Ni_x^{2+}Cr_t^{3+}Al_z^{3+}Fe_{1-z-t}^{3+})^{B}O_4$ with

Fig. 8. (A) Optical image of horizon F with laminae F′ and F‴. The chert vein crossing horizon F is highlighted by dashed lines. The black box represents the area scanned by the proton beam (5 mm × 0.5 mm) by steps of 20 μm (250 × 25 pixels). PIXE images of Fe, Ni and Cr are shown on the bottom. (B) Projection on x-axis of data for Fe and Ni. Each compositional result was obtained from the fitting of the spectra grouped over the 25 vertical pixels for each horizontal position of the beam. Data corresponding to lamina F′ and F‴ and the vein are delineated by blue, red and green vertical lines, respectively. (For interpretation of the references to colour in this figure legend, the reader is referred to the web version of this article.)

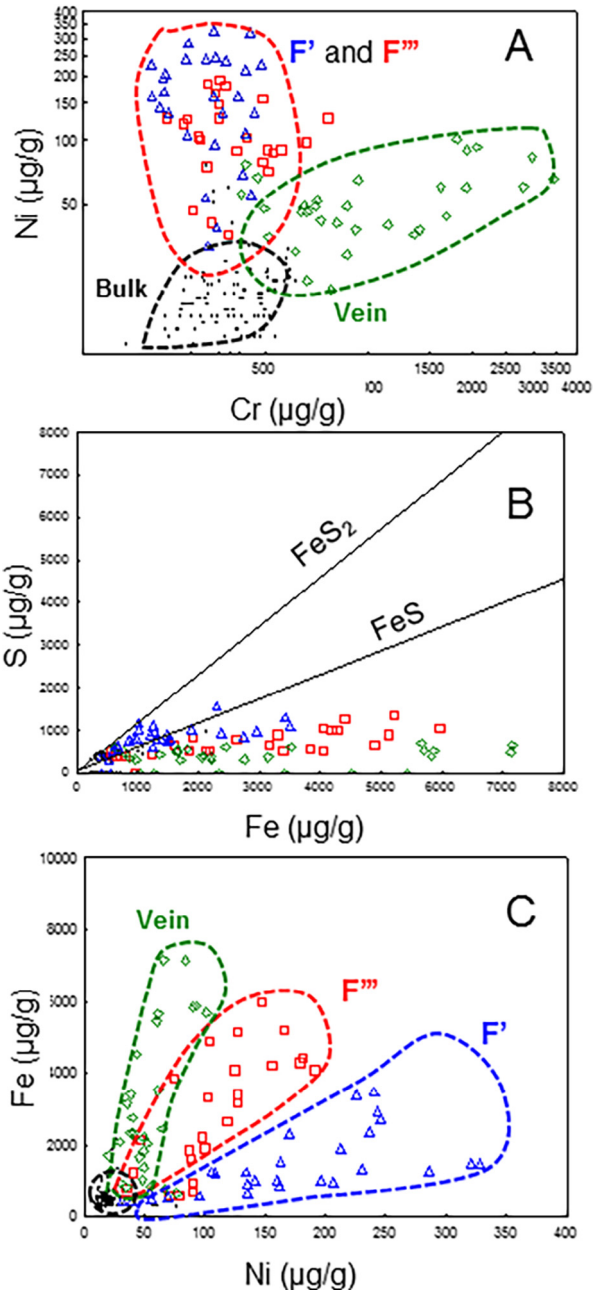

Fig. 9. Scatter plots of Ni/Cr (A), S/Fe (B) and Fe/Ni (C) PIXE analysis of sample α, which show the distinction between laminae F′ (blue triangles) and F‴ (red squares), the vein (green diamonds), and the surrounding tuffaceous layers (bulk, black points). (For interpretation of the references to colour in this figure legend, the reader is referred to the web version of this article.)

$0 \le x \le 1$ and $0 \le z + t \le 1$. This composition can be formally written in terms of a mixture of single ion oxides as: (1-x) FeO + x NiO + z/2 Al_2O_3 + t/2 Cr_2O_3 + (1-z/2-t/2) Fe_2O_3. To reduce the number of degrees of freedom and, considering that $NiFe_2O_4$ (trevorite) and $Fe^{2+}(Fe^{3+})_2O_4$ (magnetite) are inverse spinels (Fleet, 1981; Patange et al., 2011), Fe^{2+} and Ni^{2+} were constrained to occupy the B sites only. The g-values and spin number for each ion are given in Table 1.

Table 1
g-factor and electron spin S of transition metal elements in A and B sites of spinel structure.

	Fe^{3+}		Fe^{2+}	Ni^{2+}	Cr^{3+}
Site	A	B	B	B	B
g-factor	2.0	2.0	2.1	2.3	2.0
Spin S	5/2	5/2	2	1	3/2

For a fixed value of chromium content t, Eq. (1) with $g = \pm 3$ yields a linear relationship between the Al content z and the Ni content x, and non-linear relationships between $Fe^{3+}/Fe_{total} = (2 - z - t)/(3 - x - z - t)$ and the Ni content x. Details of the calculation are given in Supplementary Information D. From these relationships, a first graph can be drawn correlating the Fe^{3+}/Fe_{total} ratio with the NiO content for a range of Al content z and Cr content t (blue dots, Fig. 10A). Another graph in Fig. 10B correlates the weight percent of Al_2O_3 with the weight percent of NiO for fixed values of chromium content t (full lines for $g = +3$ and dashed lines for $g = -3$). These graphs define iron redox ranges and Al, Ni and Cr composition ranges of a spinel which give $|g| = 3$. In particular this g-value is possible only for Fe^{3+}/Fe_{total} larger than 50%, depending on the NiO content (Fig. 10A). Although a EPR line with $|g| = 3$ can occur for a broad range of Al_2O_3, NiO and Cr_2O_3 compositions (full lines and dashed lines in Fig. 10B), this g-value cannot occur in the composition range below the line defined by $[Al_2O_3] = -0.565\,[NiO] + 13$ (dotted line in Fig. 10B).

The fact that the Fe^{3+}/Fe_{total} must be larger than 50% to give spinels with $|g| = 3$ explains why such g-values have not been observed in terrestrial spinels, which exhibit low Fe^{3+} content. As an example, the green rectangles in Fig. 10 represent the composition range of 3.24 Ga Archaean detrital spinels from eroded komatiitic volcanic rocks, measured by electron microprobe (Krull-Davatzes et al., 2010). It appears that the Fe^{3+}/Fe_{total} ratio as well as the Al_2O_3 and Cr_2O_3 contents of these spinels are clearly outside the existence domains of $|g| = 3$. On the contrary, cosmic spinels identified in a spherule bed in the K-T boundary (Robin et al., 1992, 1993), represented by the pink areas of Fig. 10, show too high Fe^{3+}/Fe_{total} ratios and too low NiO contents to give an EPR signal at $|g| = 3$. Concerning Archaean, Krull-Davatzes et al. (2010) analyzed the composition of cosmic spinels in the 3.24 Ga impact spherule bed S3, Fig Tree Group of the BGB. Their composition range is represented by the blue areas in Fig. 10. Interestingly, the large domain of experimental Fe^{3+}/Fe_{total} versus NiO content (blue area in Fig. 10A) measured for these Archaean cosmic spinels intersects the calculated curves (blue dots in Fig. 10A) for NiO content between 10 and 20 wt% and Fe^{3+}/Fe_{total} in the range 55–80 % (Fig. 10A). This compatibility of the $|g| = 3$ signal of horizon F with the composition measured for Archaean cosmic spinels is supported by the correlation between Al_2O_3 content and NiO content for various Cr_2O_3 contents (Fig. 10B). Comparison of the $|g| = 3$ existence domain with actual compositions of Archaean cosmic spinels shows that a part

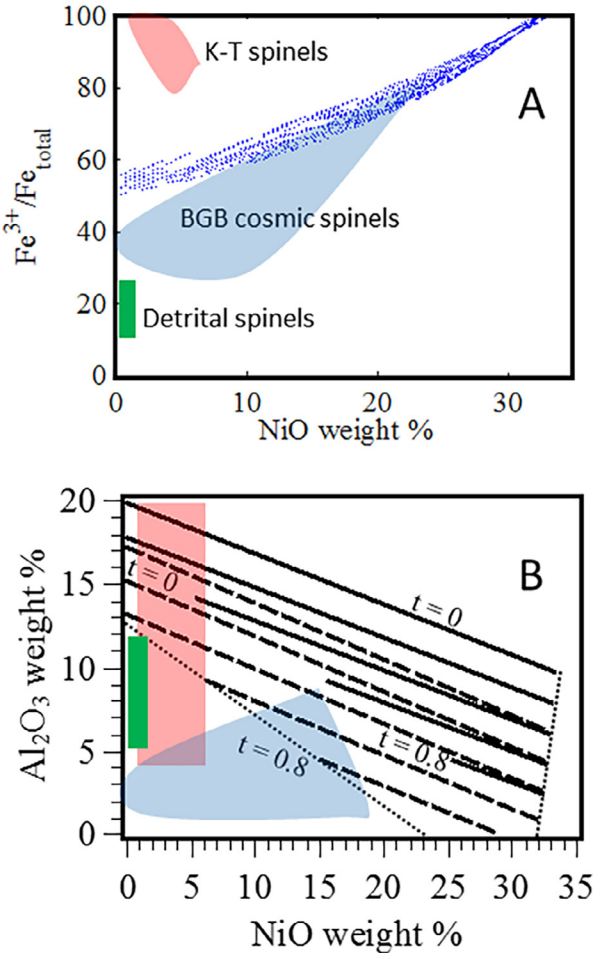

Fig. 10. Chemical composition of a Ni-Cr-Al ferrite spinel compatible with $g = \pm 3$. (A) The bundle of blue lines represent the Fe^{3+} to total Fe ratio *vs* NiO weight percent for varying values of chromium content t between 0 and 1 and varying values of aluminum content z, calculated from Eqs. (B.5a), (B.5b), and (B.7) to (B.9) of Appendice B. (B) Al_2O_3 weight percent *vs* NiO weight percent for varying chromium content t between 0 and 1 by steps of 0.2. Full and dashed lines correspond to $g = +3$ (Eq. (B.5a)) and $g = -3$ (Eq. (B.5b)), respectively. The domain in which the $|g| = 3$ lines exist is delimited by dotted lines. Blue areas represent values measured by electron microprobe analysis of cosmic spinels in 3.24 Ga impact spherule beds S3 in the Barberton Greenstone Belt (BGB; Krull-Davatzes et al., 2010). Pink areas represent values measured for cosmic spinels of the K-T boundary (Robin et al., 1992, 1993). Green rectangles represent the average composition of detrital spinels derived from the erosion of 3.24 Ga komatiitic volcanic rocks (Krull-Davatzes et al., 2010). (For interpretation of the references to colour in this figure legend, the reader is referred to the web version of this article.)

of the latter should exhibit a g factor $g = -3$ (intersection of the blue area with dashed lines for $t = 0.6$ and 0.8 in Fig. 10B) for NiO contents of 10–20 wt% and for high Cr content (the t values between 0.6 and 0.8 in Fig. 10B correspond to 22–29 weight% of Cr_2O_3, respectively). It should be pointed out that these NiO contents (~10–20 %) of cosmic spinels compatible with $|g| = 3$ in Fig. 10A and 10B were derived independently, suggesting that our deductions are coherent. However the Cr_2O_3 content calculated for a $g = -3$ line (22–29%) is lower than the effective Cr_2O_3 content of 30–55% measured for the cosmic spinels of the S3 spherule bed (Krull-Davatzes et al., 2010). Despite this discrepancy, the experimental correlation curve between Fe^{3+}/Fe_{total} and Cr_2O_3 established by these authors (Fig. 6 of Krull-Davatzes et al., 2010) shows that cosmic spinels with our Fe^{3+}/Fe_{total} values in the range 55–80 % (the case of F horizon) would exhibit Cr_2O_3 contents in the range ~15–30%, which fits very well with our calculated values of 22–29 % necessary to attribute the $|g| = 3$ EPR signal to Ni-Cr-Al-Fe spinels.

Cosmic spinels are formed by a high degree of melting of the object as it falls towards the Earth's surface, with Fe^{3+}/Fe_{total} ratios mainly determined by the O_2 fugacity of the atmosphere (Toppani and Libourel, 2003). Krull-Davatzes et al. (2010) observed that, although the BGB cosmic spinels show a large dispersion of Fe^{3+}/Fe_{total} and NiO contents, there is a positive correlation between Fe^{3+}/Fe_{total} and NiO. This is naturally imposed by the fact that Ni^{2+} ions replace Fe^{2+} ions in the spinel structure. Hence, an increase in Fe^{3+}/Fe_{total} implies a higher NiO content. This correlation is clearly shown by the bundle of calculated curves characterizing a $|g| = 3$ line in the diagram of Fig. 10A (blue dots). Taken together, the curves in Fig. 10A and the comparison with the experimental Fe redox and Ni contents found in BGB cosmic spinels (Fig. 7 in Krull-Davatzes et al., 2010) point to a low atmospheric oxygen fugacity of $10^{-5} < f_{O2} < 10^{-4}$ bar for obtaining the spinel composition deduced for horizon F of the Josefsdal Chert. These values are compatible with the oxygen-poor Archaean atmosphere. On the other hand, the Fe^{3+}/Fe_{total} and NiO content of spinels from K-T spherules (pink area in Fig. 10A) correspond to a present day, oxygen-rich, atmosphere (Toppani and Libourel, 2003), and exclude EPR signals with $g = 3$.

Finally, it is important to note that the EPR line at $|g| = 3$ is sufficiently narrow to be detectable in horizon F, which indicates that the corresponding spinel are superparamagnetic, implying that the size of these particles is at most a few tens of nm (Griscom, 1984). For larger particles, the EPR signal would be broadened and distorted (ferromagnetic resonance), which would strongly limit their detection at low concentrations (Griscom, 1984).

In summary the coexistence, in horizon F of the Josefsdal Chert, of hydrogenated organic matter of chondritic origin and cosmic spinel nanoparticles is a strong line of evidence that this sedimentary layer contains a relatively high concentration of materials of extraterrestrial origin.

5. DISCUSSION

This EPR analysis of a thin, carbonaceous horizon in 3.33 Ga-old strata sediments from Facies D of the Josefsdal Chert, Barberton Greenstone Belt, shows two independent spectroscopic features pointing to an extraterrestrial origin of a fraction of the preserved organic and inorganic matter:

(i) The cw-EPR lineshape and linewidth of IOM in horizon F of Facies D are similar to those of carbonaceous chondrites, but different from those of IOM preserved in cherts from other Archean formations, including Facies C of the Josefsdal Chert (Fig. 6). This finding is confirmed by pulse-EPR (HYSCORE) analysis of the IOM of horizon F, which exhibits ^{1}H and ^{13}C signals with characteristics similar to those of IOM of carbonaceous chondrites (Gourier et al., 2013). The presence of a ^{31}P signal, a biosignature (Gourier et al., 2013), is also present indicating that the IOM in horizon F is a mixture of two components: biogenic IOM (hereafter referred to as B-IOM) similar to that present in other parts of the Josefsdal Chert (e.g. Westall et al., 2015), and extraterrestrial IOM (hereafter referred to as E-IOM) similar to that present in carbonaceous chondrites.

(ii) An anomalous cw-EPR signal at $g = 3$ in horizon F is attributed to Ni-Cr-Al ferrite nanoparticles, co-located with the E-IOM. Their chemical composition is compatible with cosmic spinels produced by extraterrestrial materials entering the Archaean Earth's atmosphere.

It is difficult to envisage a single impact event preserving both organic matter and spinel particles in such a thin sedimentary layer. On the one hand, hydrogenated organic matter can survive only if the temperature of the falling matter does not exceed a few hundred degrees. On the other hand, cosmic spinels are formed by a high degree of melting of the object, as it falls towards the Earth's surface. In such conditions, the organic matter would be invariably destroyed. It must be stressed that the evidence of impact events during the Archaean is mainly deduced from the presence of spherule beds. On this basis, at least 8 major impactor events (>10 km diameter) are documented in sediments of the BGB between 3.47 and 3.24 Ga, occurring at a frequency of about one impactor every 30 Ma (Lowe et al., 2014; Lowe and Byerly, 2018). One of these impactors (S6) is located in the slightly younger M3c chert, stratigraphically just above the Josefsdal chert (the stratigraphic equivalent of K3c in Lowe et al., 2014), and apparently caused significant destruction due to tsunamis. The breccia beds below and above Facies D may have had a related origin (Westall et al., 2015). While large impactors show clear geological signatures on the Early-Mid Archaean record (tsunamis, spherule beds), smaller impactors were much more abundant, but would have produced more discrete signatures, such as slumping and liquefaction, either directly from impact shock and/or through associated seismic activity. Today, the largest flux of extraterrestrial materials falling on Earth is represented by micrometeorites (Prasad et al., 2013; Love and Brownlee, 1991; Dartois et al., 2018 and references therein). Similarly, the flux of extraterrestrial materials during the Archaean, much larger than today, was also certainly largely dominated by micrometeorites (cf Maurette and Brack, 2006). However, such tiny particles leave no evident geological trace of their presence. Importantly, the temperature reached by submillimeter particles during atmospheric entry strongly depends on their size. Love and Brownlee (1991) calculated that temperatures can reach 1500 °C for the largest particle sizes, allowing melting and spinel formation (Toppani and Libourel, 2003), while particles with sizes smaller than 10 μm experience sufficiently low temperature to allow organic matter to survive. Consequently it appears likely that a continuous flow of micrometeorites falling on the Archean Earth provided an enormous quantity of extraterrestrial materials, among which cosmic spinels and E-IOM represent two extreme poles. It would therefore not be surprising to find both cosmic spinels and E-IOM in Archaean sediments, intermixed with B-IOM and volcanic materials. Thus, it is strongly suspected that such E-IOM and cosmic spinels could be present in the whole of all the Josefsdal Chert formation, however in amounts too small to be detected by EPR or other analytical techniques because diluted by the other components. In our opinion, what is exceptional is not the finding of extraterrestrial material in Archaean sediments, but the fact that, during a very short period of time (corresponding to the deposition of F horizon), the proportion of extraterrestrial materials was sufficiently high to be detectable.

We thus propose that a cloud of particles, mixing volcanic ash and extraterrestrial materials, was present in the ambient atmosphere above the Josefsdal volcanic island. A specific concatenation of circumstances, detailed below, then led to a brief concentration of the extraterrestrial materials in one particular sedimentary layer. This scenarios does not exclude the likelihood that extraterrestrial materials containing both E-IOM and spinel particles in these sediments, may also result from the reworking and weathering of previous micrometeorite falls. What could the first-order control on the local concentration of E-IOM and cosmic spinels in a near-shore volcano sedimentary formation? Comparison with modern ashfall deposits (Orton, 1996; Mastin et al., 2009; Kratzmann et al., 2010) suggests that an ≈10 cm thick bundle of tephra (representing one eruptive phase), resulting from multiple eruptive pulses (events), is probably deposited in several hours to days, and the whole of the 0.6–1.2 m thick unit of green-grey and black laminated sediments (Unit 3/Facies D, Fig. 1) could have been deposited on a scale of weeks to months. The thin F horizon deposition that concerns us, which can be traced stratigraphically for several kilometers, was deposited in a very short time and immediately buried by the following thin ash layer and thus sealed without being reworked by currents or waves. If our scenario of windblown debris from micrometeorite falls is correct, carbonaceous layers slightly above and below the section analyzed could possibly be enriched to various degrees in E-IOM.

The scenario that we propose is the following. Facies D was formed primarily by passive settling of volcanic ash during explosive activity, the ash clouds comprising mostly volcanic material as well as extraterrestrial materials from continuous flux of micrometeorites. During passive settling in the water, the heaviest particles sediment first, followed the lightest ones, resulting in the vertical graded texture observed in facies D. Thus the finest part of the ash cloud,

including the extraterrestrial components, would settle out last. As a matter of fact, the presence of very fine particles in the atmosphere induces the condensation of water droplets, forming a fine rain. Consequently it was only during a very short and quiet period of remission between volcanic events, combined with no current or wave activity, that the dust was gently deposited. In such a geological setting, the presence of extraterrestrial dust would be detectable only because these conditions were present simultaneously, resulting in a local concentration of extraterrestrial material in horizon F. Under more agitated conditions (strong current and wave action and ashfall), the extraterrestrial dust would have been dynamically intermixed with and diluted by volcanic ash in the atmosphere and in the sediments, thus preventing its detection by EPR.

Importantly, the preservation of hydrogenated E-IOM in 3.33 Ga-old sediment indicates that the molecular structure of the organic precursors was partially preserved for more than 3 billion years owing to the rapid silicification and lithification of the sedimentary layers. This hypothesis may appear counterintuitive, as it is well documented that the H/C ratio of IOM decreases with increasing maturation (see Vandenbroucke and Largeau, 2007 for a review). As both biogenic and meteoritic organic matter trapped in the Archean sediment underwent the same thermodynamic and kinetic conditions (temperature, pressure, time), they should be at the same stage of maturation and, in particular, should exhibit the same amount of hydrogen loss. The fact that B-IOM has lost its hydrogen (facies C, for example) while E-IOM (horizon F of facies D) conserved a significant hydrogen fraction indicates that differences in molecular structure of the organic precursor may be an important factor controlling its geological evolution (Vandenbroucke and Largeau, 2007). We suggest that the highly branched character of aliphatic chains in chondritic IOM (Gardinier et al., 2000; Derenne and Robert, 2010) could have hindered or slowed down their aromatization. Thus, for steric reasons, some C-H bonds could have been preserved in the E-IOM, while the more linear (less branched) organic chains in precursors of biological origin (mainly lipids) implies that their aromatization (and therefore hydrogen loss) may occur more readily for the same steric reasons. This hypothesis needs to be tested by laboratory experiments (accelerated maturation of E-IOM and of biogenic B-IOM) but suggests the exciting possibility that the memory of the origin of the organic precursor could be identified by EPR analysis of IOM even after several billion years.

Our documentation of the physical presence of E-IOM in early terrestrial sediments is significant in that it underlines the importance of the flux of extraterrestrial carbon to the early Earth, already modelled to be high, $\sim 5 \times 10^{24}$ g accreted in the 300 My after the Moon-forming impact (e.g. Maurette and Brack, 2006). The high content of carbon molecules in micrometeorites, comprising both soluble organic matter (ESOM), such as PAHs and amino acids, as well as IOM, would have supplied the early Earth with a major fraction of organic material necessary for seeding the emergence of life (Brack et al., 2011; Dartois et al., 2018). As we have seen above, this extraterrestrial matter is so fine that it is readily disseminated in the seawater and in the sediments deposited in the early oceans. Incorporated in the sediments, the ESOM will have been rapidly dissolved while the more refractory E-IOM fraction would have formed part of the sediments. Recycling of the sediments containing E-IOM by tectonic activity, combined with hydrothermal leaching within the upper crust, would have resulted in cracking of the molecules to form smaller entities, expelled by hydrothermal fluids into the seawater and sediments adjacent to hydrothermal vents, that could participate in the prebiotic processes leading to the emergence of protolife or primitive cells (Westall et al., 2018).

6. CONCLUSIONS

We have shown that a 1 mm-thick lamina of carbonaceous matter in rhythmically-graded tuffaceous sediments deposited in a littoral (shoreface to upper shoreface) environment exhibits EPR characteristics of IOM signature (cw-EPR spectrum lineshape and linewidth; pulse-EPR (HYSCORE) spectrum of ^{1}H and ^{13}C) that are similar to those observed in the IOM of carbonaceous chondrites. These extraterrestrial IOM signatures are co-located with the EPR signature of submicrometric-sized particles of Ni-Cr-Al ferrite spinels, which can be formed during entry of extraterrestrial objects into an oxygen-poor atmosphere. We conclude that there is strong evidence for extraterrestrial influence in 3.33 Ga-old volcanic sediments from the Josefsdal Chert. The IOM-rich laminae represent the tops of upward-fining sequences of airborne volcanic ash. Optical microscopy and EPR study of all carbon-rich laminae in the sample analyzed suggests that, apart from the particular lamina (F′) in question, the carbonaceous matter is of terrestrial biological origin. In lamina F′ the IOM is significantly diluted by extraterrestrial carbon.

The detection of extraterrestrial carbonaceous matter in Early Archean sediments underlines the importance of the flux of extraterrestrial carbon to the early Earth from the Hadean onwards, as soon as the surface of the planet became habitable, and its contribution to the prebiotic processes that led to the emergence of life. The co-existence of two phases of carbon, one extraterrestrial and one biogenic, in the same sedimentary deposit emphasizes the challenges facing *in situ* study of carbonaceous materials on other planetary bodies, such as Mars, where the search for traces of life is primarily based on the characteristics of the organic matter and where an extraterrestrial component has already been revealed (Eigenbrode et al., 2018).

ACKNOWLEDGMENTS

We express our gratitude to Cécile Engrand and the other two reviewers for their illuminating comments and reviews which have greatly improved the text, calling our attention on many details that needed to be clarified. We also acknowledge funding from the French Space Agency (CNES) and from the European Community's Seventh Framework Programme (FP7/2007-2013) under Grant Agreement no 607297 (MASE project). We thank C. Pacheco for giving access to the Accélérateur Grand Louvre pour l'Analyse Elémentaire (AGLAE) facility and Q. Lemasson, L. Pichon and B. Moignard for their help with the PIXE measure-

ments. Support from the EPR research network RENARD (FR-CNRS 3443) for providing access to the pulse EPR equipment is gratefully acknowledged. We thank Yann Le Du for his help in the sample preparation.

APPENDIX A. SUPPLEMENTARY DATA

Supplementary data to this article can be found online at https://doi.org/10.1016/j.gca.2019.05.009.

REFERENCES

Barnes S. J. and Roeder P. L. (2001) The range of spinel compositions in terrestrial mafic and ultramafic rocks. *J. Petrol.* **42**, 2279–2302.

Binet L., Gourier D., Derenne S. and Robert F. (2002) Heterogeneous distribution of paramagnetic radicals in insoluble organic matter from the Orgueil and Murchison meteorites. *Geochim. Cosmochim. Acta* **66**, 4177–4186.

Binet L., Gourier D., Derenne S., Robert F. and Ciofini I. (2004) Occurrence of abundant diradicaloid loieties in the insoluble organic matter from the Orgueil and Murchison meteorites: a fingerprint of its extraterrestrial origin ? *Geochim. Cosmochim. Acta* **68**, 881–891.

Boehnke P. and Harrison T. M. (2016) Illusory late heavy bombardments. *Proc. Natl. Acad. Sci. U.S.A.* **2; 113**(39), 10802–10806.

Botis S. M. and Pan Y. (2009) Theoretical calculations of $[AlO_4/M^+]^0$ defects in quartz and crystal-chemical controls on the uptake of Al. *Min. Mag.* **73**, 537–550.

Bottke W. F., Vokrouhlicky D., Minton D., Nesvorny D., Morbidelli A., Brasser R., Simonson B. and Levison H. F. (2012) An Archean heavy bombardment from a destabilized extension of the asteroid belt. *Nature* **485**, 78–81.

Bourbin M., Gourier D., Derenne S., Binet L., Le Du Y., Westall F., Kremer B. and Gautret P. (2013) Dating carbonaceous matter in Archean cherts by Electron Paramagnetic Resonance. *Astrobiology* **13**, 151–162.

Brack A. (2011) *Extraterrestrial delivery of organic compounds*. Springer, pp. 821–828.

Byerly G. R. and Lowe D. R. (1994) Spinels from Archean impact spherules. *Geochim. Cosmochim. Acta* **58**, 3469–3486.

Calligaro T., Coquinot Y., Pichon L. and Moignard B. (2011) Advances in elemental imaging of rocks using the AGLAE external microbeam. *Nucl Instr. and Meth. B* **269**, 2364–2372.

Campbell J. L., Boyd N. I., Grassi N., Bonnicka P. and Maxwell J. A. (2010) The Guelph PIXE software package IV. *Nucl Instr. and Meth. B* **268**, 3356–3363.

Cooper G. W., Kimmich N. and Belizle W., et al. (2001) Carbonaceous meteorites as a source of sugar-related organic compounds for the early Earth. *Nature* **414**, 879–883.

Cosmidis J., Benzerara K., Guyot F., Skouri-Panet F., Duprat E., Férard C., Guigner J. M., Babonneau F. and Coelho C. (2015) Calcium-phosphate biomineralization induced by alkaline phosphataseactivity in Escherichia coli: Localization, kinetics, and potential signatures in the fossil records. *Front. Earth Sci.* **3**, article 84.

Dartois E., Engrand C., Duprat J., Godard M., Charon E., Delauche L., Sandt C. and Borondics F. (2018) Dome C ultracarbonaceous Antarctic micrometeorites Infrared and Raman fingerprints. *A & A* **609**, A65.

Delpoux O., Gourier D., Vezin H., Binet L., Derenne S. and Robert F. (2011) Biradical character of the D-rich carriers in the insoluble organic matter of carbonaceous chondrites : a relic of the protoplanetary chemistry. *Geochim. Cosmochim. Acta.* **75**, 326–336.

Derenne S. and Robert F. (2010) Model of molecular structure of the insoluble organic matter isolated from Murchison meteorite. *Meteoritic Planet. Sci.* **45**, 1461–1475.

Dickneider T. A., Scull S., Whelan J. K. and Blough N. V. (1997) EPR study of kerogens from Middle Valley, Northern Juan de Fuca Ridge. *Org. Geochem.* **26**, 341–352.

Duchesne J., Depireux J. and Litt C. (1964) Concerning the nature of free radicals in the Cold Bokkeveld meteorite. *Geoch. Int.* **1**, 1022–1024.

Duprat J., Dobrica E., Engrand C., Aléon J., Marrocchi Y., Mostefaoui S., Meibom A., Leroux H., Rouzaud J. N., Gounelle M. and Robert F. (2010) Extreme deuterium excesses in ultracarbonaceous micrometeorites from central Antarctic snow. *Science* **328**, 742–745.

Eigenbrode J. L., Summons R. E., Steele A., Freissinet C., Millan M., Navarro-González R., Sutter B., McAdam A. C., Franz H. B., Glavin D. P., Archer, Jr., P. D., Mahaffy P. R., Conrad P., Hurowitz J. A., Grotzinger J. P., Gupta S., Ming D. W., Sumner D. Y., Szopa C., Malespin C., Buch A. and Coll P. (2018) Organic matter preserved in 3-billion-year-old mudstones at Gale crater, Mars. *Science* **360**, 1096–1101.

Fleet M. E. (1981) The structure of magnetite. *Acta Cryst.* **B37**, 917–920.

Foucher F., Guimbretière G., Bost N. and Westall F. (2017) *Petrographical and mineralogical applications of raman mapping* (Chapter 8). InThechOpen Limited, London, pp. 163–180.

Gardinier A., Derenne S., Robert F., Behar F., Largeau C. and Maquet J. (2000) Solid state CP/MAS ^{13}C NMR of the insoluble organic matter of the Orgueil and Murchison meteorites: quantitative study. *Earth Planet. Sci. Lett.* **184**, 9–21.

Gayraud J., Robin E., Rocchia R. and Froget L. (1996) Formation condition of oxidized Ni-rich spinel and their relevance to the K/T boundary event. *Geol. Soc. Am. Spec. Pap.* **307**, 425–443.

Genda H., Brasser R. and Mojzsis S. J. (2017) The terrestrial late veneer from core disruption of a lunar -sized impactor. *Earth Planet. Sci. Lett.* **480**, 25–32.

Glikson A. Y., Allen C. and Vickers J. (2004) Multiple 3.47-Ga-old asteroid impact fallout units, Pilbara Craton, Western Australia. *Earth Planet. Sci. Lett.* **221**, 383–396.

Gomes R., Levison H. F., Tsiganis K. and Morbidelli A. (2005) Origin of the cataclysmic Late Heavy Bombardment period of the terrestrial planets. *Nature* **435**, 466–469.

Gorter E. W. (1954) Ionic distribution deduced from the g-factor of a ferrimagnetc spinel: Ti4+ in fourfold coordination. *Nature* **173**, 123–124.

Gourier D., Robert F., Delpoux O., Binet L., Vezin H., Moissette A. and Derenne S. (2008) Extreme deuterium enrichment of organic radicals in the Orgueil meteorite: revisiting the interstellar interpretation? *Geochim. Cosmochim. Acta* **72**, 1914–1923.

Gourier D., Delpoux O., Skrzypczak-Bonduelle A., Binet L., Ciofini I. and Vezin H. (2010) EPR, ENDOR and HYSCORE study of the structure and the stability of vanadyl-porphyrin complexes encapsulated in silica: Potential paramagnetic biomarkers for the origin of life. *J. Phys. Chem. B* **114**, 3714–3725.

Gourier D., Delpoux O., Binet L. and Vezin H. (2013) Nuclear magnetic biosignatures in the carbonaceous matter of ancient cherts: comparison with carbonaceous meteorites. *Astrobiology* **13**, 932–947.

Govindaraju K. (1982) Report (1967–1981) on four ANRT rock reference samples: diorite DR-N, serpentine UB-N, bauxite BX-N and disthène DT-N. *Geostandards Newsletter* **6**(1), 91–159.

Griscom D. L., Beltran-Lopez V., Merzbacher C. I. and Bolden E. (1999) Electron spin resonance of 65-million-year-old glasses and rocks from the Cretaceous-Tertiary boundary. *J. Non-Cryst.Solids* **253**, 1–22.

Griscom D. L. (1980) Ferromagnetic resonance of fine grained precipitates in glass: a thumbnail review. *J. Non-Crystalline Solids* **42**, 287–296.

Griscom D. L. (1984) Ferromagnetic resonance of precipitated phases in natural glasses. *J. Non-Crystalline Solids* **67**, 81–118.

Kratzmann D. J., Carey S. N., Fero J., Scasso R. A. and Naranjo J. A. (2010) Simulations of tephra dispersal from the 1991 explosive eruptions of Hudson volcano, Chile. *J. Volcanol. Geoth. Res.* **190**, 337–352.

Krull-Davatzes A. E., Byerly G. R. and Lowe D. R. (2010) Evidence of a lowe-O2 Archean atmosphere from nickel-rich chrome spinels in 3.24 impact spherules, Barberton greenstone belt South Africa. *Earth Planet. Sci. Lett.* **296**, 319–328.

Li J., Benzerara K., Bernard S. and Beyssac O. (2013) The link between biomineralization and fossilization of bacteria: insights from field and experimental studies. *Chem. Geol.* **359**, 49–69.

Love S. G. and Brownlee D. E. (1991) Heating and thermal transformation of micrometeoroids entering the Earth's atmosphere. *Icarus* **89**, 26–43.

Lowe D.R., Byerly G.R. and Heubeck C. Geologic map of the west-central Barberton Greenstone Belt: Geological Society of America Map and Chart Series MCH103, 1 sheet, scale 1:25 000, 2012.

Lowe D. R., Byerly G. R. and Kyte F. T. (2014) Recently discovered 3.42-3.23 Ga impact layers, Barberton Belt, South Africa: 3.8 Ga detrital zircons, Archean impact history, and tectonic implications. *Geology* **42**, 747–750.

Lowe D. R. and Byerly G. R. (2018) The terrestrial record of Late Heavy Bombardment. *New Astron. Rev.* **81**, 39–61.

Mastin I. G., Guffanti M., Servranckx R., Webley P., Barsotti S., Dean K., Durant A., Ewert J. W., Neri A., Rose W. I., Schneider D., Siebert I., Stundert B., Swanson G., Tupper A., Volentik A. and Waythomas C. F. (2009) A multidisciplinary effort to assign realistic source parameters to models of volcanic ahs-cloud transport and dispersion during eruptions. *J. Volcanol. Geoth. Res.* **186**, 10–21.

Marty B., Alexander C. M. O. D. and Raymond S. N. (2013) Primordial origins of Earth's carbon. *Rev. Mineral. Geochem.* **75**, 149–181.

Maurette M. and Brack A. (2006) Cometary petroleum in Hadean time? *Meteorit. Planet. Sci.* **41**, 5247.

Montanari A., Hay R. L., Alvarez W., Asaro F., Michel H. V., Alvarez L. W. and Smit J. (1983) Spheroids at the Cretaceous-Tertiary boundary are altered impact droplets of basaltic composition. *Geology* **11**, 668–671.

Morbidelli A., Lunine J. I., O'Brien D. P., Raymond S. N. and Walsh K. J. (2012) Building terrestrial planets *Annu. Rev. Earth Planet. Sci.* **40**, 251–275.

Mrozowski S. (1988a) ESR study of carbonization and coalification processes part I: carbonaceous compounds. *Carbon* **26**, 521–529.

Mrozowski S. (1988b) ESR study of carbonization and coalification processes part II: biological materials. *Carbon* **26**, 531–541.

Orton G. J. (1996) Volcanic environments. In *Sedimentary Environments: Processes, Facies and Stratigraphy* (ed. H. G. Reading). Wiley, p. 704.

Pasek M. and Lauretta D. (2008) Extraterrestrial flux of potential prebiotic C, N and P to the early Earth. *Orig. Life Evol. Biosph.* **38**, 5–21.

Patange S. M., Shirsath S. E., Jangam G. S., Lohar K. S., Jadhav S. S. and Jadhav K. M. (2011) Rietveld structure refinement, cation distribution and magnetic properties of Al^{3+} substituted $NiFe_2O_4$ nanoparticles. *J. Appl. Phys.* **109**, 053909.

Pichon L., Moignard B., Lemasson Q., Pacheco C. and Walter P. (2014) Development of a multi-detector and a systematic imaging system on the AGLAE external beam. *Nucl Instr. and Meth. B* **318**, 27–31.

Pinti D. L. (2005) The formation and evolution of the oceans. In *Lectures in Astrobiology* (eds. M. Gargaud, B. Barbier, H. Martin and J. Reisse). Springer, Berlin.

Prasad M. S., Rudraswami N. G. and Panda D. K. (2013) Micrometeorite flux on Earth during the last ~50,000 years. *J. Geophys. Res. Planets* **118**, 2381–2399. https://doi.org/10.1002/2013JE004460.

Remusat, L., 2014. Organic material in meteorites and the link to the origin of life. BIO web of conferences, 2, 03003. http://doi.org/10.1051/bioconf/20140203001.

Retcofsky H. L., Stark J. M. and Friedel R. A. (1968) Electron spin resonance in American coals. *Anal. Chem.* **40**, 1699–1704.

Robin E., Bonté Ph., Froget L., Jéhanno C. and Rocchia R. (1992) Formation of spinels in cosmic objects during atmospheric entry: a clue to the Cretaceous-Tertiary boundary event. *Earth Planet. Sci. Lett.* **108**, 181–190.

Robin E., Froget L., Jéhanno C. and Rocchla R. (1993) Evidence for a K/T impact event in the Pacific Ocean. *Nature* **363**, 615–617.

Ryan C. G. (1995) The Nuclear Microprobe as a probe of earth structure and geological processes. *Nucl. Instr. and Meth. B* **104**, 377–394.

Schmitt-Kopplin P., Gabelica Z., Gougeon R. D., Fekete A., Kanawati B., Harir M., Gebefuegi I., Eckel G. and Hertkorn N. (2010) High molecular diversity of extraterrestrial organic matter in Murchison meteorite revealed 40 years after its fall. *PNAS* **107**, 2763–2768.

Schoenberg R., Kamber B. S., Collerson K. D. and Moorbath S. (2002) Tungsten isotope evidence from ~ 3.8-Gyr metamorphosed sediments for early meteorite bombardment of the earth. *Nature* **418**, 403–405.

Schultz K. F. and Elofson R. M. (1965) Electron spin resonance of organic matter in the Orgueil meteorite. *Geochim. Cosmochim. Acta.* **29**, 157–160.

Schweiger A. and Jeschke G. (2001) *Principle of Pulsed Electron Paramagnetic Resonance*. Oxford University Press, Oxford.

Sephton M. A. (2002) Organic compounds in carbonaceous meteorites. *Natl. Prod. Rep.* **19**, 292–311.

Simonson B. M. and Glass B. P. (2004) Spherule layers – records of ancient impacts. *Ann. Rev. Earth Planet. Sci.* **32**, 329–361.

Skrzypczak-Bonduelle A., Binet L., Delpoux O., Vezin H., Derenne S., Robert F. and Gourier D. (2008) EPR of radicals in primitive organic matter: a tool for the search of biosignatures of the most ancient traces of life. *Appl. Magn. Reson.* **33**, 371–397.

Smart J. S. (1954) Cation distribution in mixed ferrites. *Phys. Rev.* **94**, 847–850.

Smit J. and Kyte F. T. (1984) Siderophile-rich magnetic spheroids from the Cretaceous-Tertiary boundary in Umbria, Italy. *Nature* **310**, 403–405.

Strasdeit H. (2005) New studies on the Murchison meteorite shed light on the pre-RNA world. *ChemBioChem* **6**, 801–813.

Tartèse R., Chaussidon M., Gurenko A., Delarue F. and Robert F. (2017) Warm Archean oceans reconstructed from oxygen isotope composition of early-life remnants. *Geochem. Persp. Let.* **3**, 55–65. https://doi.org/10.7185/55 geochemlet.1706.

Toppani A. and Libourel G. (2003) Factors controlling compositions of cosmic spinels: Application to atmospheric entry conditions of meteoritic materials. *Geochim. Cosmochim. Acta* **67**, 4621–4638.

Uebersfeld J., Etienne A. and Combrisson J. (1954) Paramagnetic resonance, a new property of coal-like materials. *Nature* **174**, 614.

Uebersfeld J. and Erb E. (1956) A new effect of oxygen on the paramagnetic resonance of charcoal. *Comptes Rendus Acad Sci. (Paris)* **243**, 363–364.

Vandenbroucke M. and Largeau C. (2007) Kerogen origin, evolution and structure. *Org. Geochem.* **38**, 719–833.

Vinogradov A. P., Vdovykin G. P. and Marov I. N. (1964) Free radicals in the Miggei meteorite. *Geoch. Int.* **1**, 395–398.

Wertz J. E. and Bolton J. R. (1986) *Electron Spin Resonance: Elementary Theory and Practical Applications*. Chapman and Hall, New York.

Westall F., de Ronde C. E. J., Southam G., Grassineau N., Colas M., Cockell C. and Lammer H. (2006) Implications of a 3.472-3.333 Gyr-old subaerial microbial mat from the Barberton greenstone belt, South Africa for the UV environmental conditions on the early Earth. *Phil. Trans. R. Soc. B* **361**, 1857–1875.

Westall F., Cavalazzi B., Lemelle L., Marrocchi Y., Rouzaud J. N., Simionovici A., Salome M., Mostefaoui S., Andreazza C., Foucher F., Toporski J., Jauss A., Thiel V., Southam G., MacLean L., Wirick S., Hofmann A., Meibom A., Robert F. and Defarge C. (2011) Implications of in situ calcification for photosynthesis in a ~3.3 Ga-old microbial biofilm from the Barberton Greenstone Belt, South Africa. *Earth Planet. Sci. Lett.* **310**, 468–479.

Westall F., Campbell K. A., Bréhéret J. G., Foucher F., Gautret P., Hubert A., Sorieul S., Grassineau N. and Guido D. M. (2015) Archean (3.33 Ga) microbe-sediment systems were diverse and flourished in a hydrothermal context. *Geology* **43**, 615–618.

Westall F., Hickman-Lewis K., Hinman N., Gautret P., Campbell K. A., Bréhéret J. G., Foucher F., Hubert A., Sorieul S., Dass A. V., Kee T. P., Georgelin T. and Brack A. (2018) A hydrothermal-sedimentary context for the origin of life. *Astrobiology* **18**, 1–35.

Weeks R. A., Magruder, III, R. H. and Stesman A. (2008) Review of some experiments in the 50 year saga of the E' center and suggestions for future research. *J. Non-Cryst. Solids* **354**, 208–216.

Weil J. A. (1984) A review of Electron Spin Spectroscopy and its application to the study of paramagnetic defects in crystalline quartz. *Phys. Chem. Miner.* **10**, 149–165.

Yada T., Nakamura T., Takaoka N., Noguchi T., Terada K., Yano H., Nakazawa T. and Kojima H. (2004) The global accretion rate of extraterrestrial materials in the last glacial period estimated from the abundance of micrometeorites in Antarctic glacier ice. *Earth Planets Space* **56**, 67–79.

Associate editor: Christian Koeberl